Monthly Notices of the ROYAL ASTRONOMICAL SOCIETY

MNRAS **503,** 1753–1772 (2021)
Advance Access publication 2021 February 4

doi:10.1093/mnras/stab249

Flat rotation curves of $z \sim 1$ star-forming galaxies

Gauri Sharma,[1,2,3,4★] Paolo Salucci,[1,2,3★] C. M. Harrison,[5] Glenn van de Ven[4★] and Andrea Lapi[1,3]

[1] *SISSA International School for Advanced Studies, Via Bonomea 265, I-34136 Trieste, Italy*
[2] *QGSKY, INFN-Sezione di Trieste, via Valerio 2, I-34127 Trieste, Italy*
[3] *IFPU Institute for Fundamental Physics of the Universe, Via Beirut, 2, I-34151 Trieste, Italy*
[4] *Department of Astrophysics, University of Vienna, Türkenschanzstrasse 17, A-1180 Wien, Austria*
[5] *School of Mathematics, Statistics and Physics, Newcastle University, Newcastle upon Tyne NE1 7RU, UK*

Accepted 2021 January 24. Received 2020 December 21; in original form 2020 April 30

ABSTRACT

We investigate the shape of the rotation curves (RCs) of $z \sim 1$ star-forming galaxies (SFGs) and compare them with local SFGs. For this purpose, we have used 344 galaxies from the *K*-band Multi-Object Spectrograph (KMOS) for Redshift One Spectroscopic Survey (KROSS). This sample covers the redshift range $0.57 \leq z \leq 1.04$, the effective radii $0.69 \leq R_e$ [kpc] ≤ 7.76, and the stellar masses $8.7 \leq \log(M_*\,[\mathrm{M}_\odot]) \leq 11.32$. Using ^{3D}BAROLO, we extract the Hα kinematic maps and corresponding RCs. The main advantage of ^{3D}BAROLO is that it incorporates the beam smearing in the 3D observational space, which provide us with the intrinsic rotation velocity even in the low spatial resolution data. We have corrected the RCs for pressure support, which seems to be a more dominant effect than beam smearing in high-z galaxies. Only a combination of the three techniques (3D-kinematic modelling + 3D-beam smearing correction + pressure gradient correction) yields the intrinsic RC of an individual galaxy. Further, we present the co-added and binned RCs constructed out of 256 high-quality objects. We do not see any change in the shape of RCs with respect to the local SFGs. Moreover, we notice a significant evolution in the stellar-disc length (R_D) of the galaxies as a function of their circular velocity. Therefore, we conclude that the stellar disc of SFGs evolves over cosmic time (from $z \sim 1$) while the total mass stays constant (within ∼20 kpc).

Key words: galaxies: disc – galaxies: evolution – galaxies: kinematics and dynamics – dark matter.

1 INTRODUCTION

In the late 1980s, Rubin, Ford Jr & Thonnard (1980) and Bosma (1981) published the most explicit observational evidence of non-Keplerian Rotation Curves (RCs) of spiral galaxies. These findings have made far-reaching changes in the field of Astronomy, Astrophysics as well as Cosmology, introducing an elusive component that astrophysicist dubbed as Dark Matter, thought to made of a dark particle necessarily beyond the standard model of elementary particles. Since then, Dark Matter (DM) became a building block of the current cosmological model so as the formation and evolution of all the structures in the Universe (Padmanabhan 1993; Springel et al. 2005). It contributes ≈ 24 per cent to the energy budget of the Universe (Freedman & Turner 2003), despite 'no success' in the discovery of its particle nature.

In the local Universe, by studying the shape of the RCs, we established a fair understanding about the presence of DM and its contribution in the mass distribution (e.g. Salucci & Burkert 2000; Sofue & Rubin 2001; Salucci et al. 2007; Courteau & Dutton 2015; Salucci 2019, and references therein). The rotation curve studies not only constrain the mass budget but has also strengthened our understating of galaxy formation and evolution (e.g. Reyes et al. 2011; Read et al. 2016; Karukes & Salucci 2017; Lapi, Salucci & Danese 2018b). On the basis of observational evidence of the DM in the local Universe, and the development in the field of (1) high-resolution numerical simulations and (2) large galaxy surveys, those could identify the structures and substructures hosting galaxies and measure their spatial clustering. The current galaxy formation and evolution scenario suggest a theoretical account of DM halo, in which baryonic matter collapses to form the stars and a subsequent growth leads to the formation of a galaxy (Wechsler & Tinker 2018, references therein).

In the last decade, advanced use of integral field units (IFUs) in galaxy surveys has opened the several possibilities of studying the spatially resolved kinematics and the dynamics of galaxies. For example, surveys with the Multi-Unit Spectroscopic Explorer (MUSE; Bacon et al. 2010), *K*-band Multi-Object Spectrograph (KMOS; Sharples 2015), and the Spectrograph for INtegral Field Observations in the Near Infrared (SINFONI; Eisenhauer et al. 2003). Usually, the kinematics of the galaxies are derived using spatially resolved emission line measurements (e.g. Hα, [O III]) extracted from the IFU data. In particular, in this work we use data from the KMOS Redshift One Spectroscopic Survey (KROSS; Stott et al. 2016), which uses the Hα emission line to trace the galaxy kinematics.

Lang et al. (2017) and Genzel et al. (2017), used IFU data from KMOS and SINFONI to analyse the RCs of $0.6 \lesssim z \lesssim 2.4$ star-forming galaxies (SFGs) and found a declining behaviour with

★ E-mail: 7.gaurisharma@gmail.com (GS); salucci@sissa.it (PS); glenn.vandeven@univie.ac.at (GvdV)

© 2021 The Author(s)
Published by Oxford University Press on behalf of Royal Astronomical Society

Downloaded from https://academic.oup.com/mnras/article/503/2/1753/6128665 by SISSA - Scuola Internazionale Superiore di Studi Avanzati user on 29 March 2021

increasing radius, in contrast to the RCs of local SFGs that are remarkably flat and rarely decline (e.g. Rubin et al. 1980; Persic, Salucci & Stel 1996). In brief, Lang et al. (2017) studied the stacked normalized RCs of 101 SFGs at $0.6 \lesssim z \lesssim 2.2$ with stellar mass $9.3 \lesssim \log(M_* [\mathrm{M}_\odot]) \lesssim 11.5$, where the normalization is performed at turn over radii, where $R_{\rm turn} \sim 1.65R_e$. Genzel et al. (2017) studied the individual RCs of six massive ($log(M_* [\mathrm{M}_\odot]) = 10.6$–$11.1$) SFGs at redshift $0.9 \leq z \leq 2.4$. They showed the declining RCs in two cases: (1) when individual RCs are normalized at $R_{\rm max}$ where the amplitude of rotation velocity is maximum and; (2) when binned averages of the six individual galaxies are normalized at the effective radii (R_e). In the end, both studies (Genzel et al. 2017; Lang et al. 2017) proposed that the declining behaviour of RCs can be explained by a combination of 'high baryon fraction' and extensive 'pressure support'.

In comparison, Tiley et al. (2019b) studied the shape of RCs of ≈1500 high-z ($0.6 \lesssim z \lesssim 2.2$) SFGs with stellar masses $8.5 \lesssim \log(M_* [\mathrm{M}_\odot]) \lesssim 11.7$. They used a similar stacking approach as Lang et al. (2017), but normalized the RCs at three times the stellar disc scale length (i.e. $3R_D$, where $R_D = 0.59R_e$), without accounting the pressure support corrections. They found flat RCs, more like those seen in the local Universe. In the end, to explain the difference in their results to those presented in Lang et al. (2017), Tiley et al. (2019b) concluded that the shape of stacked RCs depends on the choice of the normalization scale used in constructing the average RCs.

Differences in RC shapes may also arise due to different kinematic modelling approaches, different treatment of observational uncertainties (e.g. low resolution and small angular size lead to the beam smearing), and the underlying physical effects, e.g. pressure support/gradient (Valenzuela et al. 2007; Read et al. 2016; Wellons et al. 2020). In regards to the observational uncertainties, although IFUs brought remarkable progress in the field, due to the small angular size of the high-z galaxies, the attained spatial resolution is limited. Without Adaptive Optics (AO), an IFU achieves only 0.5–1.0 arcsec spatial resolution, whereas, a galaxy from $z \sim 1$ has a typical angular size of 2–3 arcsec. The finite beam size causes the line emission to smear on the adjacent pixels. This effect is referred to as 'Beam Smearing', which underestimates the rotation velocity and overestimates the velocity dispersion. The same beam smearing scenario happens in H I observations (Bosma & Van der Kruit 1979; Begeman 1989) of local spiral galaxies. Although the previous IFU studies of high-z galaxies have applied beam-smearing corrections in different ways, these have usually been applied to the derived 2D velocity maps or the 1D RCs. An alternative approach is to apply dynamical models and beam-smearing corrections simultaneously directly to the 3D data cube. For example, ^{3D}BAROLO (Teodoro & Fraternali 2015; Di Teodoro, Fraternali & Miller 2016) (hereafter BBarolo) uses a tilted ring approach, which allows the reconstruction of intrinsic kinematics closest to the observations. Then the model is compared with data ring by ring in 3D space, and, at the same time, beam smearing corrections are accounted for. This is the approach that we employ in this work and the details are discussed in Section 3.1.

In regards to varying physical galaxy properties affecting the RCs of galaxies, it is particularly important to consider that the interstellar medium (ISM) is turbulent in high-z galaxies which could modify the kinematics of the galaxies (Burkert et al. 2010; Glazebrook 2013; Turner et al. 2017; Johnson et al. 2018; Übler et al. 2019; Wellons et al. 2020) and may result in different shapes of RCs. In fact, previous studies have shown that average gas velocity dispersion evolves with redshift as well as the disc fraction (Kassin et al. 2007, 2012; Wisnioski et al. 2015, 2019; Simons et al. 2017) and dark matter content[1] (F'orster Schreiber & Wuyts 2020, and references therein). This could clearly impact upon the shape of the RCs that are derived from kinematic measurements of high-z galaxies.

As mentioned earlier in the section, the kinematics of the galaxies are derived using the emission lines like H α or [O III]. These emission lines arise from the gaseous disc around the stars or the ISM. If the ISM is highly turbulent, then the emission also experiences a turbulence, i.e. radial force against gravity. This turbulence/force scales with the gas density and velocity dispersion. Since the density and velocity dispersion both decrease with increasing radius, this creates a pressure gradient, i.e. $F_P \propto -\mathrm{d}P/\mathrm{d}r$ (where $P \propto \rho\sigma^2$). The resulting radial force supports the disc and makes it rotate slower than the actual circular velocity, which might result in declining the RCs and potentially underestimate the dynamical masses (Valenzuela et al. 2007; Dalcanton & Stilp 2010). This effect is generally minimal in the local rotation-dominated SFGs but significant in the local dwarfs and early-type galaxies (e.g. Valenzuela et al. 2007; Weijmans et al. 2008; Read et al. 2016). Since, high-z SFGs are gas dominated (Glazebrook 2013; Tacconi et al. 2018, references therein), and the ISM is relatively turbulent (F'orster Schreiber & Wuyts 2020, references therein). Therefore, it is essential to take into account the pressure gradient. In this work, we apply the 'Pressure Gradient Correction' (PGC) on RCs, as mentioned in the Section 3.2.

The article is organized as follows: In Section 2, we describe the sample used in this work; Section 3 contains a brief discussion on the kinematic modelling using ^{3D}BAROLO code and PGCs; in the Sections 4 and 5, we have discussed the main results, shown the shape of RCs, and their comparison with the locals RCs; Section 6 contains a summary of the work. In this work, we have assumed a flat ΛCDM cosmology with $\Omega_{m,0} = 0.27$, $\Omega_{\Lambda,0} = 0.73$, and $H_0 = 70\,\mathrm{km\,s^{-1}}$.

2 DATA

KMOS-Redshift One Spectroscopic Survey (KROSS) was aimed to observe the $z \sim 1$ SFGs (Stott et al. 2016). In this work, we have analysed a subsample of the publicly available KROSS data to determine the 'intrinsic RCs' of high-z rotation dominated SFGs (most likely disc-type galaxies). The minor and major details of observations and physical properties of the full sample can be found in Stott et al. (2016) and other first and foremost papers by the KMOS team (e.g. Harrison et al. 2017; Johnson et al. 2018; Tiley et al. 2019b). Nevertheless, in the section below, we have given a short overview of KROSS and our sample selection criteria.

2.1 KMOS observations

KROSS is an integrated field spectroscopic (IFS) survey using the KMOS instrument on ESO/VLT. The KMOS consists of 24 Integrated Field Units (IFUs); those can be placed within 7.2 arcmin diameter field. Each IFU covers the $2.8 \times 2.8\,\mathrm{arcsec}^2$ in size with 0.2 arcsec pixels. The targets for the survey are selected from extragalactic deep field covered by multiwavelength photometric and spectroscopic data: (1) Extended Chandra Deep Field Survey (E-CDFS; Giacconi et al. 2001; Lehmer et al. 2005), (2) Cosmic Evolution Survey (COSMOS; Scoville et al. 2007), (3) Ultra-Deep Survey (UKIDSS; Lawrence et al. 2007), (4) SA22 field (Steidel et al.

[1] A recent study by Genzel et al. (2020) shows that the dark matter versus baryonic matter contribution to the RCs may be different at different redshifts.

Downloaded from https://academic.oup.com/mnras/article/503/2/1753/6128665 by SISSA - Scuola Internazionale Superiore di Studi Avanzati user on 29 March 2021

1998). Some of the targets were selected from CF-HiZELS survey (Sobral et al. 2015). The targets were selected such that the Hα emission is shifted into *J* band. The median redshift of parent sample (KROSS full sample) is $z = 0.85^{+0.11}_{-0.04}$. The median *J* band seeing of observations was 0.7 arcsec, with 92 per cent of the objects were observed during seeing <1 arcsec. Individual frames have exposure times of 600 s, and a chop to the sky was performed every two science frames. The data were reduced using ESOREX/SPARK pipeline (Davies et al. 2013), and flux calibration is performed using standard stars which have been observed during the same night as science data. The end product of the process is 3D datacube which consists of two spatial axes and one spectral axis of 2048 channels (e.g. 3D datacube = $f(x, y, \lambda)$). These datacubes are capable of producing spectrum, the line, and the continuum images and the moment maps (see: Stott et al. 2016). Since mid-2019, these data are publicly available at KROSS-website.[2]

2.2 KROSS sample selection

We are focusing on 586 KROSS galaxies studied by Harrison et al. (2017, hereafter H17), we refer it as parent sample. We have selected 344 objects out of 586, on the basis of integrated Hα flux cut ($F_{\rm H\alpha} > 2 \times 10^{-17}$ [erg s^{-1} cm^{-2}]) and inclination angle ($25^\circ \leq \theta_i \leq 75^\circ$). The chosen flux and inclination cuts ensure the sufficient signal-to-noise data (S/N) and reduces the impact of extinction[3] during the kinematic modelling procedure (see Section 3.1). The intrinsic characteristic of the selected sample (referred to as 'analysed sample') is the following (given with respect to table A1 of H17): (1) AGN-flag is zero, i.e. no evidence for an AGN contribution to the Hα emission-line profile; (2) H17 Quality-flag 1, 2, and 3, i.e. only Hα-emission line detected objects ($S/N > 3$). We adopted the values of effective radii (R_e), photometric position angle (PA), photometric inclination angle (θ_i), absolute *H*-band magnitude (M_H), *K*-band AB magnitude ($K_{\rm AB}$), z-band AB magnitude ($z_{\rm AB}$), Hα luminosity ($L_{\rm H\alpha}$), Hα flux ($F_{\rm H\alpha}$), Hα star-formation rate ($\rm SFR_{H\alpha}$), and redshift (z). For the details of adopted quantities, we refer the reader to Harrison et al. (2017) and Stott et al. (2016), while next we briefly discuss some of the requisite quantities.

The position angle (PA) and inclination angle (θ_i) are estimated by fitting a 2D Gaussian model to the broad-band images. Harrison et al. (2017) compared their PA and θ_i with van der Wel et al. (2012) which fits Sérsic models to the *HST* near-infrared images using GALFIT that incorporates PSF modelling. Their calculations were in agreement with the GALFIT results and those derived using a 2D Gaussian fitting method. Moreover, PA and θ_i for COSMOS targets with *I*-band images were cross-checked with Tasca et al. (2009) who derived the PA and θ_i using the axis ratios.

The effective radii (R_e) is measured from the broad-band images by deconvolving the PSF and semimajor axis of the aperture, which contains half of the total flux. Since the broad-band images are observed in *I*, z', *H*, and *K* bands (depends on the surveys goal and instrument facility) therefore, the targets where the images are in *I*, and z' band, a systematic correction factor of 1.1 is applied in R_e to account the colour gradient. The simple approach of colour correction applied because *HST* images were not available for all the targets (for details see Harrison et al. 2017).

To obtain the galaxy integrated Hα luminosity ($L_{\rm H\alpha}$), Harrison et al. (2017) first grade the Hα sources on the basis of signal-to-noise (S/N: average over two times derived velocity full width at half-maximum (FWHM) of Hα line). If the S/N $\leq$3, then sources are discarded. Secondly, the emission line width is corrected for instrumental dispersion, which is measured from unblended skylines near the observed wavelength of the Hα emission. Then, the Hα flux was measured using 2.5 arcsec aperture (with an uncertainty of 30 per cent) and hence the integrated Hα luminosity[4] obtained.

The stellar masses are derived using the LE PHARE (Arnouts et al. 1999; Ilbert et al. 2006) spectral energy distribution (SED) fitting tool. The LE PHARE compares the suits of modelled SED of object from observed SED. Where observed SED of our sample is derived from optical and NIR photometric bands (*U*, *B*, *V*, *R*, *I*, *J*, *H*, and *K*), in some cases we have also used the IRAC mid-infrared bands. In modelling, the stellar population synthesis model is derived from Bruzual & Charlot (2003) and stellar masses are calculated using Chabrier (2003) initial mass function (IMF). The LE PHARE routine fits the extinction, metallicity, age, star-formation, and stellar masses and allows for a single burst, exponential decline, and constant star formation histories. For details of stellar mass computation, we refer the reader to Tiley et al. (2019a).

We remark, the parent sample is selected in such a way that it does not preferentially contain galaxies in a merging or interacting state, and include good representatives of main sequence SFGs at $z \sim 1$ (see Stott et al. 2016, and references therein). To reaffirm, we present the distributions of the physical quantities (namely, $F_{\rm H\alpha}$, θ_i, z, R_e, M_*, and $\rm SFR_{H\alpha}$) of the parent and analysed sample, which are shown in Fig. 1. In the Appendix Fig. A1, we additionally provide the distribution of the $L_{\rm H\alpha}$ and absolute *H*-band magnitude. In short, our analysed sample covers the following range of the Hα flux: $-16.70 \leq \log(F_{\rm H\alpha}$ [erg s^{-1} cm^{-2}]) ≤ -15.26, the inclination angle: $25^\circ \leq \theta_i \leq 75^\circ$, the redshift: $0.75 \leq z \leq 1.04$, the effective radii: $-0.16 \leq \log(R_e$ [kpc]) ≤ 0.89, the stellar mass: $8.79 \leq \log(M_*$ [M$_\odot$]) ≤ 11.32, and the star formation rate:$0.15 \leq \log(\rm SFR_{H\alpha}$ [M$_\odot$ yr^{-1}]) ≤ 1.76. The final analysed sample selected for this study is representative of the parent sample from Harrison et al. (2017) and, therefore, is representative of main sequence, star-forming galaxies at this redshift.

3 METHODS

To obtain the intrinsic shape of the RCs, we follow the 3D-forward modelling and a relatively rigorous approach is considered for handling the observational and the physical uncertainties. Under 3D-forward modelling, a simulated datacube is populated for given initial conditions and then compared with the observed datacube. We keep on populating/reconstructing the simulated datacube by changing the initial guess until convergence between data and model occur. This yields the PV-diagrams and moment maps. For implementing such 3D-forward kinematic modelling of datacubes, we have used ^{3D}BAROLO code (Teodoro & Fraternali 2015), it is discussed in the section below. In the end, we implement the pressure support correction on ^{3D}BAROLO generated RCs, which is discussed in the Section 3.2.

[2]http://astro.dur.ac.uk/KROSS/data.html

[3]In the highly inclined system ($\theta_i > 75^\circ$) observed flux extinct due to extinction, which suppress the rotation velocity upto a few times R_e (see Valotto & Giovanelli 2003). On the other hand, in face-on galaxies ($\theta_i < 25^\circ$) the rotation signal drops below the observational uncertainties. Therefore, to be conservative we down-select the sample for $25^\circ \leq \theta_i \leq 75^\circ$.

[4]Notice, we do not account for extinction due to lack of required data (e.g. Balmer line ratios) to measure the extinction. However, these luminosities are not used for the bulk of our analyses.

Downloaded from https://academic.oup.com/mnras/article/503/2/1753/6128665 by SISSA - Scuola Internazionale Superiore di Studi Avanzati user on 29 March 2021

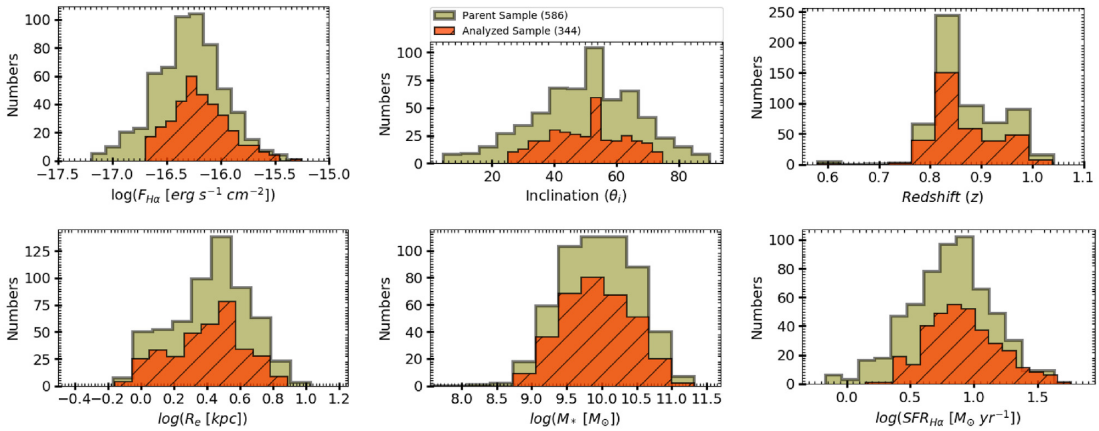

Figure 1. The distributions of physical quantities of parent and analysed sample. The colour code is same in all the panels and given as follows, the parent KROSS sample (given by Harrison et al. 2017) shown by the green histograms and the analysed sample by orange hatched histogram. The upper left and middle panel represents the $F_{\mathrm{H}\alpha}$ and θ_i distribution, which verifies our sample selection cuts. Upper right-hand panel shows the redshift (z) distribution, this justify that we are working with $z \sim 1$ galaxies. Lower left-hand panel demonstrate the size distribution of our analysed sample. The lower middle and right-hand panel shows the distribution of stellar masses and Hα based star-formation rate (SFR), these distributions are informative of main sequence at $z \sim 1$.

3.1 Kinematic modelling with ^{3D}BAROLO

We have modelled the kinematics of our sample using the ^{3D}BAROLO code (Teodoro & Fraternali 2015). The main advantage of modelling the datacube with ^{3D}BAROLO (BBarolo): (1) it allows us to reconstruct the intrinsic kinematics in 6-domain (three spatial and three velocity components) for given initial conditions; (2) the 3D projected modelled datacube is compared to the observed datacube in 3D space; (3) it simultaneously incorporates the instrumental and the observational uncertainties (e.g. spectral-smearing[5] and beam-smearing[6]) in 3D space. For details, we refer the reader to Teodoro & Fraternali (2015) and Di Teodoro et al. (2016). This 3-fold approach of deriving kinematics is designed to overcome the observational and instrumental effects and hence allows us to stay close to the realistic conditions of the galaxy. Therefore, it gives us somewhat improved results than the 2D approach of kinematic modelling on the datacubes, specifically, in the case of small angular sizes and moderate S/N of high-z galaxies (see Di Teodoro et al. 2016). In the section below, we have discussed the BBarolo's underlying assumptions, its initial requirements for performing the kinematic modelling, and the very first results/tests on a large data set.

3.1.1 *Basic assumption under ^{3D}BAROLO*

BBarolo is based on the 'tilted ring model,' i.e. the motion of the gas and stars are assumed to be in the circular orbits. It does not assume any functional evolution of the kinematic quantities (e.g. $v_{\mathrm{rot}}(R) \propto \arctan(R)$). Therefore, free parameters in BBarolo are not forced to follow any parametric form, rather estimated in the annuli of increasing distance from the galaxy centre without making any assumption on their evolution with the radius. However, BBarolo uses the radial binning for the velocity measurement, because in the 'tilted ring model', a galaxy is divided into several rings and parameters are calculated within each ring. The number of pixels used per bin depends on the choice of NRADII[7] and RADSEP[8] in the fitting. Therefore, each position–velocity (PV) diagram contains ∼3–6 rotation velocity measurements (and similarly for the velocity dispersion). The errors on velocity measurement per radial bin (inside BBarolo) are estimated using Monte Carlo sampling.

A non-parametric approach of calculating kinematic parameters, makes BBarolo robust and reliable to use, and this is one of the reasons we are using it for kinematic modelling. There are other high-z 3D-kinematic modelling codes, e.g. `GALPAK 3D` (Bouché et al. 2015), which has been successfully tested on $z \sim 0.5$ galaxies observed from the Multi-Unit Spectroscopic Explorer (MUSE) but it follows the parametric approach and `BLOBBY3D` (Varidel et al. 2019), which has been tested on 20 local star-forming galaxies from the SAMI galaxy survey. It is a useful tool to study the gas dynamics of high- z low-resolution data. However, it comes with a long list of free parameters, which one may not know without a detailed study of the system and will be particularly degenerate for lower S/N data available for high redshift systems.

3.1.2 *Initial requirements of ^{3D}BAROLO*

The kinematic modelling with BBarolo requires three geometrical parameters, i.e. the coordinates of galactic centre in the datacube (x_c, y_c), the inclination angle (θ_i), the position angle (PA), and three kinematic parameters, i.e. the redshift (z), the rotation velocity (v_{rot}) and the velocity dispersion of ionized gas ($\sigma_{\mathrm{H}\alpha}$). In our modelling, we fix the geometrical parameters and redshift (with an exception for PA, discussed below) and leave the two kinematic parameters free. Notice, (x_c, y_c) are the photometric galactic centre positions adopted from H17. BBarolo comes with several useful features particularly necessary/useful for high-z low S/N data (see BBarolo documentation[9]). We are using `3DFIT TASK` for performing the kinematic modelling. First, BBarolo produces the mock observations on the basis of given initial conditions in the 3D observational space (x, y, λ), where (x, y) stands for the spatial axes and λ is spectral axis coordinate. These models are then fitted to the observed datacube in the same 3D space accounting for the beam smearing simultaneously. A successful run of BBarolo delivers the beam smearing corrected

[5]line spread function (LSF) which corresponds to spectral broadening
[6]the point spread function (PSF) which determines the spatial resolution
[7]Number of rings used in fitting the galaxy
[8]Separation between rings in arcsec

[9]https://bbarolo.readthedocs.io/en/latest/

Downloaded from https://academic.oup.com/mnras/article/503/2/1753/6128665 by SISSA - Scuola Internazionale Superiore di Studi Avanzati user on 29 March 2021

moment maps, the stellar surface brightness profile, the rotation curve (RC), and the dispersion curve (DC) along with the kinematic models. Notice, RCs/PV diagrams are not derived from the velocity maps, instead they are calculated directly from datacubes by minimizing $V_{\rm LOS} = V_{\rm rot} \sin\theta_i$ (of model and data). BBarolo is well tested on the local systems (e.g. Teodoro & Fraternali 2015; Korsaga et al. 2019) as well as on high-z galaxies including the KMOS data (see: Di Teodoro et al. 2016; Loiacono et al. 2019).

The PA is usually fixed to the photometric PA ($\rm PA_{phot}$) adopted from the H17 catalogue, but for ∼44 per cent of objects, $\rm PA_{phot}$ does not allow to extract PV diagram. This might be a consequence of misaligned morphological and kinematic major axis. We know the fact that photometric and kinematic PAs are not necessarily the same. That is why for these 44 per cent objects, PA is kept free and estimated from the BBarolo kinematic modelling. A short discussion and an example is shown in Appendix A and Fig. A3. In the end, we also present a quantitative measure of misaligned PAs, see Appendix A1.

3.1.3 Limitations in ^{3D}BAROLO

To obtain a good fit BBarolo requires a mask to identify the true emission region and to ignores the noisy pixels. For this purpose, we use the in-built `MASK` task with an input of either `SEARCH` or `NEGATIVE` masking. In particular, the `SEARCH` mask uses the source finder algorithm `DUCHAMP` (Whiting 2012) and hence builds a mask on the identified emission regions based on 3D reconstructed sources. This mask works very well on high S/N (clean) data if noise is Gaussian distributed among the channels. However, when the noise does not follow a Gaussian distribution, then the `SEARCH` task is unable to find the source. In this situation, we have used the `NEGATIVE` mask. It computes the noise statistics ($\sigma_{\rm noise}$) channel by channel, using only pixels with negative values, then build the mask in regions of flux > (1.5–2.5) $\sigma_{\rm noise}$. Notice, noise in negative pixels are often more Gaussian-distributed than positive pixels, especially in low S/N KMOS data, and hence returns a better estimate of noise properties.

Notice that fully exploiting the 3rd (velocity) dimension is still a caveat in the 2D/3D kinematic modelling of high-z galaxies. However, we suggest that 3D-forward modelling has a potential to provide better results than applying models to fit to 2D or 1D projections of the datacube, because it uses the full information available inside the datacube. We remark (see also Teodoro & Fraternali 2015) BBarolo corrects well for beam smearing whenever a galaxy is resolved with at least 2–3 resolution elements across and has an $S/N \gtrsim 3$. The relative errors are within 20 per cent for the rotation curve and within a factor 2 for the velocity dispersion, in the worst cases.

The errors on the data are estimated during the fitting procedure, the algorithm weights pixels based on their S/N, i.e. a pixel with a high S/N is considered more reliable and given more weight than a pixel with low S/N. The noise level is calculated directly from emission-free regions of the datacube using robust statistics (median and absolute deviation from the median). Notice, BBarolo's current error-estimation algorithm does not account for intrinsic uncertainties in the data. However, we minimized the impact of these effects by a careful selection/analysis of subsample (see Section 2.2 and 3.1.4).

Finally let us remark, extinction is complex to account in the 3D modelling therefore, it is not accounted in BBarolo. However, extinction is important in inner region of galaxies, where high-z galaxies are not resolved. At least in our sample, we do not have resolution within ∼2 kpc, where extinction dominates. In particular, we do not draw any conclusions about the inner parts of the rotation curves (see Section 4.2). Nevertheless, BBarolo's performance has been extensively tested on optical/NIR data (e.g. KROSS, KMOS^{3D}; Teodoro & Fraternali 2015; Di Teodoro et al. 2016; Korsaga et al. 2019; Loiacono et al. 2019), where it delivers remarkable results. Therefore, we expect BBarolo to perform well on our sample too; however, results are critically analysed and discarded whenever required (see Section 3.1.4).

3.1.4 Results from ^{3D}BAROLO

The analysed sample was selected on the basis of the Hα emission line flux cut ($F_{\rm H\alpha} > 2 \times 10^{-17}$ [erg s^{-1} cm^{-2}]), the inclination angle cut ($25^\circ \leq \theta_i \leq 75^\circ$), and the S/N (>3) of the Hα detection. After executing BBarolo, we have visually inspected the BBarolo outputs for quality assessment. We noticed that the best quality outputs correspond to objects with the inclination $45^\circ \leq \theta_i \leq 75^\circ$ where kinematics is derived using the `SEARCH` mask. On the other hand, worse quality is often spotted for relatively low inclination ($\theta_i < 45^\circ$) along with use of the `NEGATIVE` mask. Moreover, as per the limitations of BBarolo, objects with low S/N and $\theta_i < 45^\circ$ might be being considered as background galaxy emission, which may lead to over/underestimated rotation velocity or velocity dispersion. Therefore, to classify the quality of the galaxies, we have taken into account the S/N per pixel in the masked region, limitations of BBarolo and the participation of the mask (which gives us a direct indication of the noise level). Hence, we have assigned the quality of BBarolo outputs as the following:

(i) **Quality-1**: $45^\circ < \theta_i \leq 75^\circ$ with `SEARCH` mask and $S/N > 3$ in masked region.
(ii) **Quality-2**: $30^\circ \leq \theta_i \leq 75^\circ$ with `SEARCH` or `NEGATIVE` mask and $S/N \geq 3$.
(iii) **Quality-3**: the remaining objects.

An example of a visual representation of the Quality-1, 2, and 3 objects is shown in Fig. 2. In total, we have 120 Quality-1, 194 Quality-2, and 30 Quality-3 objects. The Quality-3 galaxies are discarded from the rotation curve analysis. We would remark, Teodoro & Fraternali (2015) have tested the performance of BBarolo on simulate data in terms of S/N, spatial/spectral resolution, and galaxy properties. They have shown that the code works well when most of the emission has $S/N \gtrsim 3$ and for inclination $30^\circ \leq \theta_i \leq 75^\circ$. All of our Quality-1 and Quality-2 objects (Q12 sample) abide these criteria, except nine galaxies those inclined between $25^\circ < \theta_i < 30^\circ$ but contain $S/N > 3$ per pixel. In the external appendix, we attach the plots of S/N per pixel of the analysed sample, and inclination is given in the catalogue released with this paper.

In Fig. 3, we have shown a few examples of BBarolo outputs. From left to right, the broad-band high-resolution image, the Hα image, the first-moment (rotation velocity) map, the second-moment (dispersion velocity) map, the rotation curve, and the dispersion curve. In detail, COL 1: the broad-band image is constructed from the ground and the space-based photometric observational data (discussed in Section 2.1). The central photometric coordinate (galactic centre: (x_c^p, y_c^p)) of the object is shown by a black cross, which is calculated by fitting the 2D Gaussian to the 2D distribution of the data. The size of each image can be inferred in terms of 10 × 10 pixel size, converted to arcsec (displayed on the bottom left-hand of the image). The size of the broad-band images varies from image-to-image due

Downloaded from https://academic.oup.com/mnras/article/503/2/1753/6128665 by SISSA - Scuola Internazionale Superiore di Studi Avanzati user on 29 March 2021

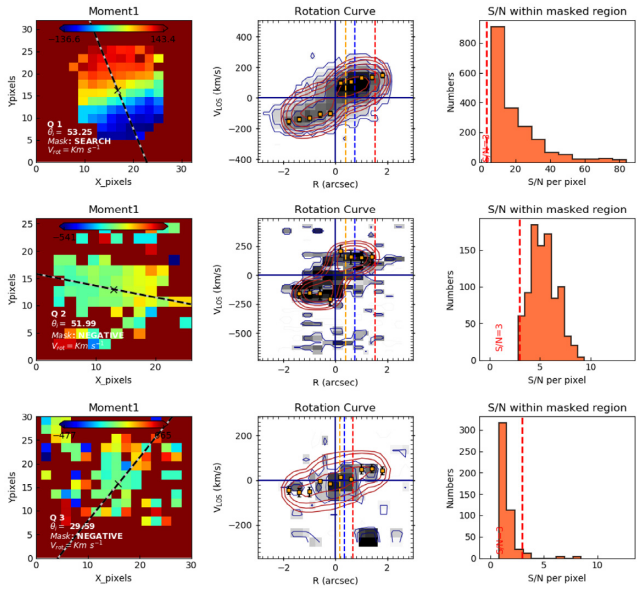

Figure 2. A visual representation of the quality assessment of BBarolo outputs. The Upper, middle, and bottom row represents the Quality-1, Quality-2, and Quality-3 galaxies, respectively. COL 1: First moment map, black-grey dashed line is showing the position angle, and the black cross shows the galactic centre (x_c^p, y_c^p). COL 2: Rotation curve, the black shaded area with blue contour shows the data while the red contour refers to the model and the orange squares with error bars are the best-fitting velocity measurements. The yellow, blue, and red vertical dashed lines are representing the effective radius (R_e), optical radius ($R_{\rm opt} = 1.89\,R_e$), twice optical radius ($R_{\rm out}$), respectively. COL 3: Distribution of S/N in masked region of datacube. The vertical red dashed line shows the $S/N = 3$.

to the multiwavelength data and different photometric surveys. COL 2: the integrated Hα-image constructed from the KMOS datacube. The size of the image is displayed in arcsec by drawing the horizontal and the vertical black line. The name of the galaxy is displayed in the upper left-hand corner, and the quality displayed in the lower left-hand corner. COL 3,4: Moment-1 map and Moment-2 map, these maps are the output of the BBarolo kinematic modelling. The black-grey dashed line shows the position angle of the image. The black cross represents the galactic centre positions adopted from the work of Harrison et al. (2017). COL 5,6: the rotation curve (RC) and the dispersion curve (DC), constructed after a comparison of the data and the model in 3D space (an output of BBarolo). In the rotation curve, the red contour is the model and the black shaded area with the blue contour represents the data. The orange squares with error bars are the best-fitting rotation velocity (referred to as 'RC data') and velocity dispersion. The yellow, blue, and red vertical dashed lines are representing the effective radius (R_e), the optical radius ($R_{\rm opt} = 1.89\,R_e$), and twice the optical radius ($R_{\rm out} = R_{\rm 2opt} = 3.78\,R_e$), respectively. The size of the Hα-image is always 2.8×2.8 arcsec^2, so are the spatial length of the moment maps, rotation, and the dispersion curve. In some cases, even though R_e is 1.6 kpc (i.e. 0.2 arcsec), RCs are extended more than 16 kpc (i.e. 2.0 arcsec) due to the fact that Hα-emission can trace the light up to large radius in comparison to broad-band filters. A full version of Fig. 3 is attached in the external appendix. Notice, BBarolo estimates the errors using Monte Carlo sampling, which are plotted on RCs and DCs in Fig. 3. In further analysis, we consider symmetric errors on RC/DC data, since parameter space is very much Gaussian distributed. However, to be precise, we take root mean square of upper and lower bounds of BBarolo estimated errors.

3.2 Pressure gradient correction

A significant amount of the BBarolo generated RCs show a strong asymmetry and rapid fall in the inner region as well as in the outskirts of the galaxy. Such a rise and fall could be either due to the low dark matter fraction or, it could be an impact of pressure support (e.g. Genzel et al. 2017). The latter is observed in local dwarfs and early-type galaxies (e.g. Valenzuela et al. 2007; Weijmans et al. 2008; Read et al. 2016), which noticeably suppresses the rotation velocity of the gas. In short, if the ISM is highly turbulent (like in high-z galaxies; Burkert et al. 2010; Turner et al. 2017; Johnson et al. 2018; Übler et al. 2019; Wellons et al. 2020), then the pressure gradient induces a force against gravity, which supports the disc against gravity and keeps it in kinematic equilibrium. This force is negligible in local rotation-dominated systems, but the same is not valid for high-z galaxies. Mainly, in the case of the dynamical mass modelling of high-z galaxies, it is very crucial to disentangle the pressure support; otherwise, one might lead to wrong estimates of baryonic and dark matter components. Therefore, to correct the azimuthal velocities for the pressure support, we follow Weijmans et al. (2008) by adopting their following pressure gradient correction (PGC):

$$V_c^2 = V_\phi^2 + \sigma_R^2 \left[-\frac{\partial\, ln\, \rho\, \sigma_R^2}{\partial\, ln\, R} + (1 - \frac{\sigma_\phi^2}{\sigma_R^2}) \right], \quad (1)$$

where V_ϕ is the inclination-corrected[10] rotation velocity, ρ is the density of gas, σ_R and σ_ϕ are the intrinsic radial and vertical velocity dispersion, respectively. Under the common assumption of a constant disc scale height the slope of the intrinsic 3D density (ρ) and 2D surface density are the same; therefore, ρ can be replaced with Σ, where Σ is 2D density[11] proportional to Hα mass surface density. From the kinematic modelling of the datacubes (discussed in Section 3.1), we have required information about Σ, σ_R and V_ϕ to employ into the PGC. Let us remark, all the quantities (namely: V_ϕ, σ_R, and Σ) are function of radius (R),[12] and they are derived from Hα datacubes.

In equation (1), the second term ($-\partial ln\ \rho\sigma_R^2/\partial ln\ R$) gives the pressure gradient and the third term ($1 - \sigma_\phi^2/\sigma_R^2$) gives the velocity anisotropy. Often, it is assumed that the velocity dispersion is isotropic, so that $\sigma_\phi = \sigma_R$. However, here, we follow Weijmans et al. (2008) in which velocity anisotropy ($1 - \sigma_\phi^2/\sigma_R^2$) is given as $(1 - \alpha)/2$, where α is the radial slope of the rotation velocity ($\alpha = \partial lnV_\phi/\partial lnR$). Therefore, we do not need to limit our formalism to isotropic velocity dispersion. Finally, equation (1) takes the form of

$$V_c^{\rm PGC} = \sqrt{V_\phi^2 - \sigma_R^2 \left[\frac{\partial ln\Sigma}{\partial lnR} + \frac{\partial ln\sigma_R^2}{\partial lnR} + \frac{1}{2}(1-\alpha) \right]}, \quad (2)$$

where $V_c^{\rm PGC}$ is the pressure gradient corrected circular velocity. Although, we assume velocity anisotropy but this term has a small effect as it is subdominant with respect to the combined slope in the density and dispersion. In Figs B1 and B2, we have shown a few examples of PGC on rising and falling RCs. Notice, BBarolo

[10]Inclination correction is required, to go from observed to intrinsic rotation velocity as well as to convert the observed velocity dispersion into the intrinsic radial dispersion in the general case of an anisotropic velocity distribution (see equation A13 of Weijmans et al. 2008).
[11]In fact, $\rho = \kappa\ \Sigma$, where κ is constant with radius.
[12]i.e. $V_\phi = V_\phi(R)$, $\sigma_R = \sigma_R(R)$, $\Sigma = \Sigma(R)$, and $\alpha = \alpha(R)$

Downloaded from https://academic.oup.com/mnras/article/503/2/1753/6128665 by SISSA - Scuola Internazionale Superiore di Studi Avanzati user on 29 March 2021

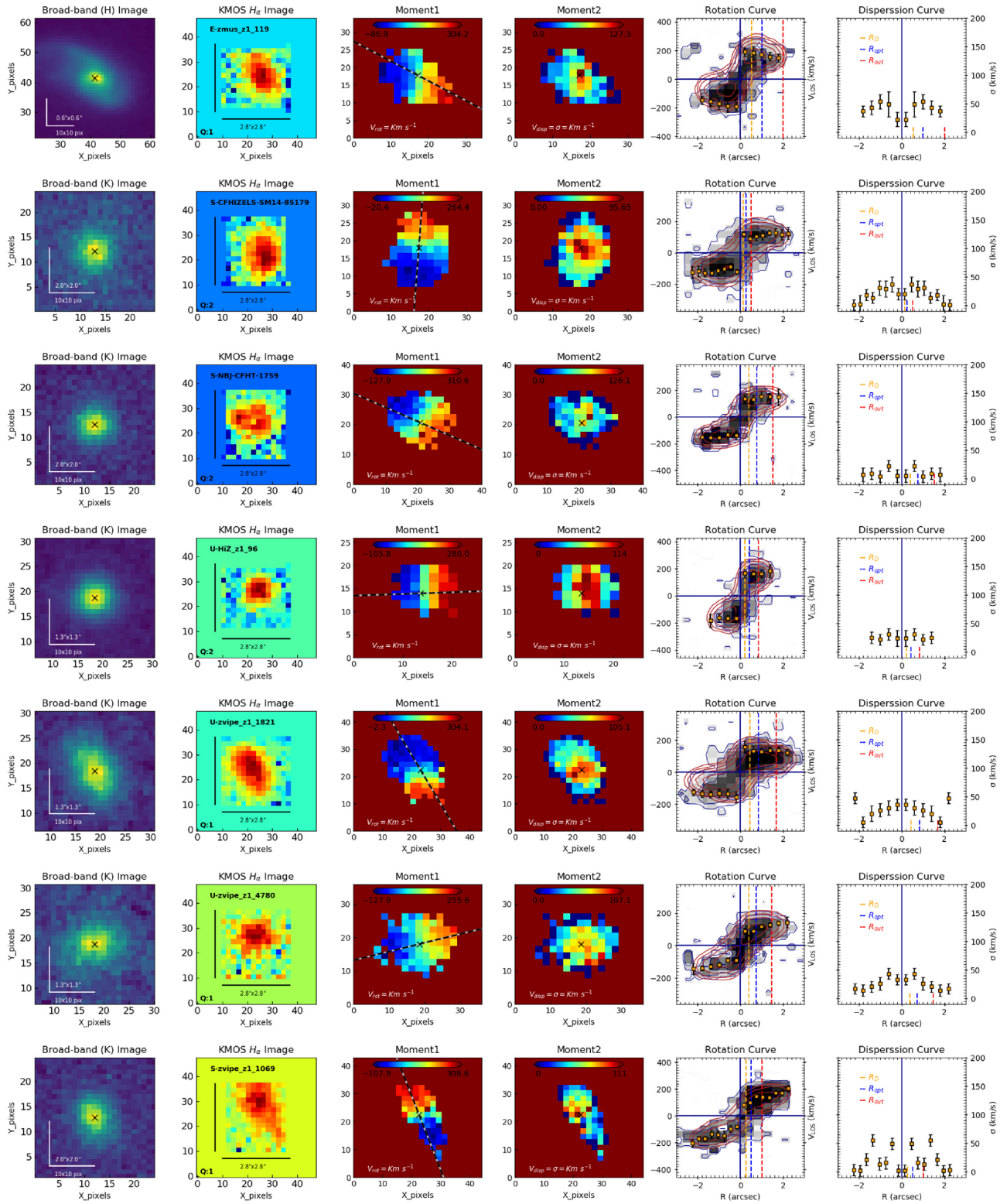

Figure 3. The outputs of the kinematic modelling using ^{3D}BAROLO. COL 1: Broad-band image, where black cross shows the central coordinates of the photometric image. The horizontal and the vertical white lines in the lower left-hand corner are showing the 10×10 pixel size in arcsec (an estimator of image size). COL 2: Integrated H α-image from datacube, the size of the image is shown by the black horizontal and the vertical lines. The name of the galaxy is shown in the upper left-hand corner, and quality is mentioned in the lower left-hand corner. COL 3–4: the first and second-moment map, the black-grey dashed line is showing the position angle, and the black cross represents the galactic centre. COL 5: Rotation curve, the black shaded area with blue contour represents the data while the red contour shows the model and the orange squares with error bars are the best-fitting rotation velocity measurements. COL 6: the best-fitting velocity dispersion. The yellow, blue, and the red vertical dashed lines are representing the effective radius (R_e), the optical radius ($R_{\rm opt} = 1.89\,R_e$), twice the optical radius ($R_{\rm out} = R_{\rm 2opt} = 3.78\,R_e$), respectively. Notice that the first data point in RCs and DCs is within resolution limit, therefore excluded from the analysis.

Downloaded from https://academic.oup.com/mnras/article/503/2/1753/6128665 by SISSA - Scuola Internazionale Superiore di Studi Avanzati user on 29 March 2021

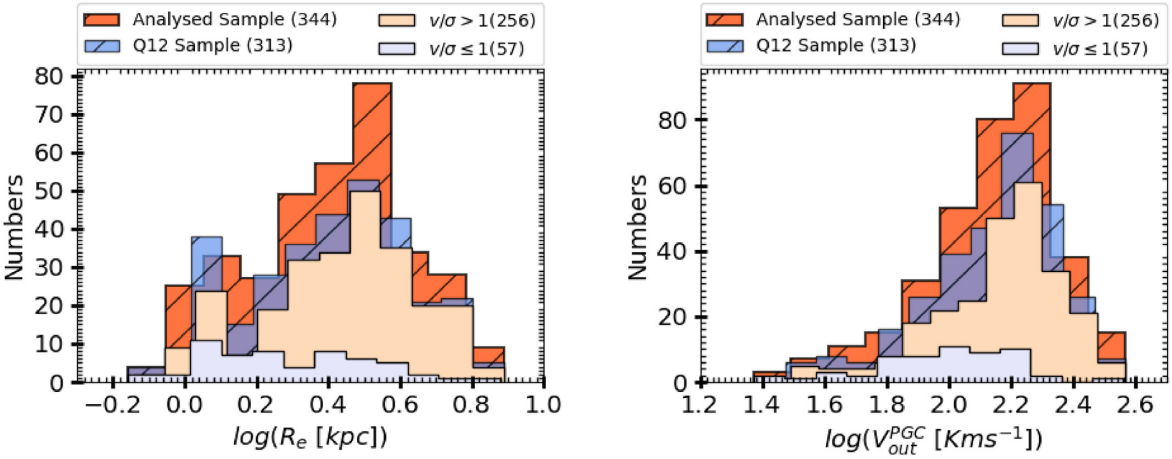

Figure 4. Left-hand panel: The effective radii distribution and Right-hand panel: the circular velocity distribution of the analysed sample. The colour codes are same in both panel and given as following: the dark orange hatched distribution is the BBarolo analysed sample, blue hatched distribution is Q12 sample (i.e. Quality-1 and 2 objects only). The peach-puff histogram represents the rotation dominated (i.e. $v/\sigma > 1$) Q12 sample, and the light blue distribution shows to the dispersion dominated (i.e. $v/\sigma \leq 1$) Q12 sample. The digits in the bracket of legend represent the total number of the objects in each subsample. In the RC analysis, we have used only rotation-dominated Q12 sample.

generated RCs are corrected for pressure support while moment-1 maps are not.

Finally let us remark, Valenzuela et al. (2007) presented a similar pressure gradient formalism as discussed above. Dalcanton & Stilp (2010), Burkert et al. (2010), and Wellons et al. (2020) apply the pressure support correction following the previous argument, but assuming the constant dispersion. Read et al. (2016) apply a correction following a similar asymmetric drift argument as Valenzuela et al. (2007), but also assuming a constant dispersion. Regarding this, we have also explored the pressure support for constant velocity dispersion (see Appendix C).

4 RESULTS

In summary, we ran BBarolo on 344 SFGs selected from KROSS survey, having the Hα flux ($F_{\rm H\alpha} > 2 \times 10^{-17}$ [erg s^{-1} cm^{-2}]), the inclination ($25^\circ \leq \theta_i \leq 75^\circ$), the redshift range ($0.75 \leq z \leq 1.04$), and the stellar masses ($8.83 \leq \log(M_*\,[{\rm M}_\odot]) \leq 11.32$). Thereby, we have 344 beam smearing corrected rotation curves, dispersion curves, and the corresponding moment maps. After quality assessment of BBarolo outputs, we have selected 314 Quality-1 and Quality-2 objects; this sample is referred to as the Q12 sample in the analysis (see Section 3.1.4). In this sample, we have 256 rotation-dominated ($v/\sigma > 1$) and 57 dispersion-dominated ($v/\sigma \leq 1$) systems, where v/σ is calculated before the PGC. A distribution of resampled data is shown in Fig. 4. This sample has objects with the effective radii $-0.16 \leq \log(R_e\,[{\rm kpc}]) \leq 0.89$ and the circular velocities $1.42 \leq \log(V_{\rm out}^{PGC}\,[{\rm km\,s^{-1}}]) \leq 2.57$.

4.1 Characteristic velocity

For an exponential thin disc, the stellar component of a galaxy follows surface density: $\Sigma_D(R) = \frac{M_D}{2\pi R_D^2} \exp\left(\frac{-R}{R_D}\right)$ (Freeman 1970), where M_D is the disc mass and R_D is the disc radius. Under this assumption, one can relate the scale length (R_e) determined from the light profile of the galaxy to compute the characteristic radius e.g. the disc length ($R_D = 0.59\,R_e$). In our work, we calculate velocities at three different characteristic radii: (1) the optical radius ($R_{\rm opt} = 3.2R_D$); (2) twice the optical radius ($R_{\rm out} = 6.4\,R_D$) and (3) R_{80}[13] i.e. the radius where the RC is presumably flat (notice that at the different radii, RCs can be rising and falling). The $R_{\rm opt}$ and $R_{\rm out}$ are the photometric measurements (derived from effective radii: R_e), whereas, R_{80} is the kinematic measurement. Referring to each radii $R_{\rm opt}$, $R_{\rm out}$, and R_{80}, we define the corresponding velocities $V_{\rm opt}$, $V_{\rm out}$ and V_{80}, respectively. In this work, we have used velocities computed at $R_{\rm out}$. The observed dispersion curves (of ionized gas) are nearly flat, therefore, we have calculated the overall velocity dispersion (σ) of the galaxy using weighted mean statistics (see equation 3). Note, the characteristic velocities measured from a PG-corrected RCs are referred to as $V_{\rm opt}^{\rm PGC}$, $V_{\rm out}^{\rm PGC}$, and $V_{80}^{\rm PGC}$, respectively. In Fig. 5, we have shown a comparison of the PGC and the non-PGC circular velocities computed at $R_{\rm out}$ ($V_{\rm out}^{\rm PGC}$ and $V_{\rm out}$, respectively). We can see that if the system does not have sufficient rotation, i.e. if $V_{\rm out}/\sigma\ (= v/\sigma) \lesssim 5$ then the pressure gradient is dominant, which is also noticeable in PG correction factor:

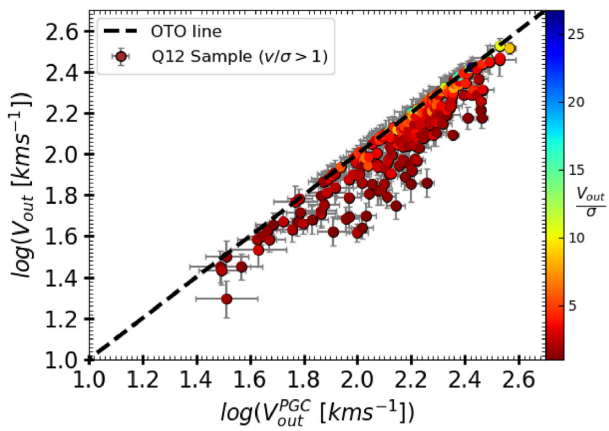

Figure 5. The correlation between rotation velocities before and after pressure gradient correction (PGC), i.e. $V_{\rm out}$ and $V_{\rm out}^{\rm PGC}$, respectively. The black dashed line shows the one-to-one relation. The objects are colour coded by $V_{\rm out}/\sigma$ ($=v/\sigma$, computed before PGC).

[13] R_{80} is the radius which covers the 80 per cent of the rotation velocity curve

Downloaded from https://academic.oup.com/mnras/article/503/2/1753/6128665 by SISSA - Scuola Internazionale Superiore di Studi Avanzati user on 29 March 2021

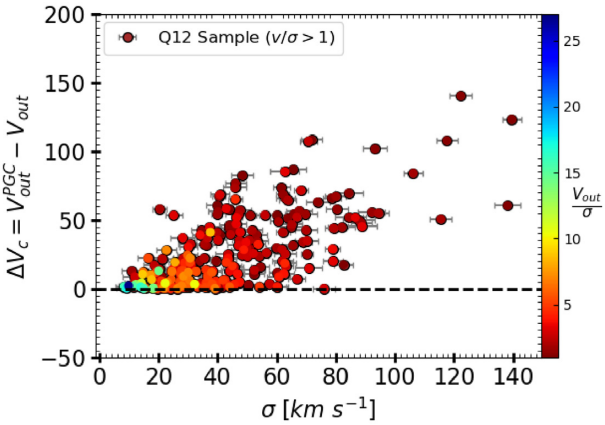

Figure 6. The pressure gradient correction factor: $\Delta V_c = V_{\rm out}^{\rm PGC} - V_{\rm out}$ as a function of velocity dispersion (σ), colour coded for $V_{\rm out}/\sigma$. The corrections are significant in $V_{\rm out}/\sigma \lesssim 5$ galaxies.

$\Delta V_c = V_{\rm out}^{\rm PGC} - V_{\rm out}$ (shown in Fig. 6). On the other hand, if the system is rotation-dominated, then the PGC does not increase the rotation velocity and hence we notice a strong correlation between $V_{\rm out}^{\rm PGC}$ and $V_{\rm out}$ for $v/\sigma > 5$.

Furthermore, we conclude that the pressure gradient is a more dominant effect in the high-z systems than the beam smearing. For a quantitative measurement, we matched RCs of our analysed sample with Harrison et al. (2017) RCs, those are not corrected for beam smearing, and calculated the rotation velocity at $3.4R_D$ in both samples (before and after PGC). We found beam smearing has increased the median rotation velocity of sample by ∼10–15 km s^{-1} (similarly observed by Johnson et al. 2018), whereas PGC increases the median rotation velocity by more than 30–50 per cent relative to the initial value. Although pressure support is dominant than beam smearing, to obtain the 'intrinsic shape of RCs', we need to correct for both effects.

4.2 Co-added rotation curves

Here, we present the five co-added and binned RCs constructed from the 256 individual RCs. We have performed co-addition on both PGC and non-PGC RCs. The technique of co-adding and binning is the following; first, we batch the RCs according to their circular velocity calculated at $R_{\rm out}$, where the dark matter is expected to be dominating. Then we treat each batch of the RCs as a single co-added RC. Secondly, we bin the galaxies radially per 2.5 kpc corresponding to the binning scale of BBarolo. For the binning, we have used standard weighted mean statistic given by

$$\bar{X} = \frac{\Sigma_{i=1}^{n} x_i \times w_i}{\Sigma_{i=1}^{n} w_i}, \tag{3}$$

where x_i = data; $\mathrm{w_i} = 1/\mathrm{error}^2$; $\bar{\mathrm{X}}$ = binned data. The errors on binned data are root mean square error, computed as $\delta_v^{r_i} = \sqrt{\sum([(\delta_{v_i}^r)^2 + (\sigma_v^{r_i})^2])/N}$, where $\delta_{v_i}^r$ is the individual error on the velocities per radial bin and $\sigma_v^{r_i}$ scatter per radial bin. We are using such a statistical approach because it has plausible advantages on the RC studies e.g. (i) it gives us a smooth distribution of RCs ignoring the random fluctuations arising from bad data points, i.e. it allows us to enhance the S/N in the data; (ii) it allows the mass decomposition of similar velocities but having different spatial sampling. This kind of approach in RC studies has been used for decades, pioneered by Persic & Salucci (1991) later developed in several other works (Persic et al. 1996; Salucci & Burkert 2000; Catinella, Giovanelli & Haynes 2006; Salucci et al. 2007; Yegorova et al. 2011; Karukes & Salucci 2017; Lapi et al. 2018b). To be more precise, we have constructed the five co-added RCs (selected according to the circular velocities at $R_{\rm out}$), where each co-added RC is divided into six radial bins. The statistics, including the number of sources included per radial and velocity bin of the co-added and binned RCs are tabulated in Table 1.

Table 1. The statistics of the co-added and binned RCs. Col. 1: shows the name of each velocity bin, e.g. bin_a-b, here a is lower velocity limit and b is higher velocity limit. Col. 2: N_v gives the number of objects per velocity bin. Col. 3 $N_{v,\,r}$ gives the number of objects per radial bin. Cols 4 and 5: gives the average $R_{\rm out}$ and $V_{\rm out}$, respectively, for the each velocity bin.

Bin name bin_V_{min}−V_{max}	N_v (dpts)	$N_{v,\,r}$ (dpts)	$\tilde{R}_{\rm out}$ (kpc)	$\tilde{V}_{\rm out}^{\rm PGC}$ (km s^{-1})
bin_50-100	36	36, 36, 36, 35, 3	12.56	80.70
bin_100-150	65	65, 65, 65, 65, 25, 5	12.24	128.04
bin_150-200	85	85, 85, 85, 85, 45, 25	11.79	175.51
bin_200-250	34	34, 34, 34, 32, 13, 3	13.31	220.67
bin_250-350	24	24, 24, 24, 24, 9, 2	14.33	277.83

In Fig. 7, we have shown the co-added and binned rotation curve before and after PGC. We notice that some of the individual RCs are subjected to large fluctuations before the PGC. In particular, the individual RCs of the lower velocity bins (bin_50-100 & $bin_100-150$) falls to zero (or stay close to zero) at $R > 4$ kpc (left-hand panel). This might be interpreted as the galaxies not being in the disc-like configuration. However, it could also be an effect of heavy turbulence (i.e. large pressure gradient), which provides a substantial pressure support, and keeps the disc in kinematic equilibrium without the need for strong rotation. We suggest that it is most likely the latter case, because after the PGC, we do not see any RC lie close to zero circular velocity (right-hand panel). This effect is also noticeable in characteristic velocity measurements (see Fig. 5) and PG correction factor (see Fig. 6) of low $v/\sigma (< 5)$ galaxies, where the corrections are ∼100–150 km s^{-1}. Here, we would like to emphasize the importance of our PGC, which makes use of complete information about the galaxy available in the datacube (namely density, dispersion, and rotation) and hence is able to correct for the strongly turbulent pressure conditions. The PGC also gives an usual shape to all RCs (as we can see in the right-hand panel of Fig. 7). Moreover, we notice that the variance (δ) in the PG corrected RCs decreased by a factor of ∼7.

We compare our binned RCs of $z \sim 1$ with the Universal Rotation Curves (URCs) of local star-forming disc-type galaxies. The URCs sample is one of the largest (contains 2300 galaxies) and deeply investigated samples, which have been used several times to show the interplay of dark and luminous matter in the local Universe (e.g. Persic & Salucci 1991; Persic et al. 1996; Salucci & Burkert 2000; Catinella et al. 2006; Salucci et al. 2007; Yegorova et al. 2011; Lapi et al. 2018b). For comparison, we have used the RCs of the same velocity bins drawn from the URC sample (particularly used in Lapi et al. 2018b). The distribution of the circular velocities of both samples is shown in Fig. 8. We notice that the circular velocities of both samples trace a similar total potential or total mass within $R_{\rm out}$. In Fig. 9, we have shown the distribution of stellar masses of both samples. Notice, for $z \sim 1$ galaxies stellar masses are derived from SED fitting while for locals (URC sample), they are derived from RC analysis given in Lapi et al. (2018b). We found that the stellar masses show a relatively broad distribution for a given velocity bin, and are noticeably lower in comparison with locals (except the lowest velocity bin). Therefore, we can state that both samples are

Downloaded from https://academic.oup.com/mnras/article/503/2/1753/6128665 by SISSA - Scuola Internazionale Superiore di Studi Avanzati user on 29 March 2021

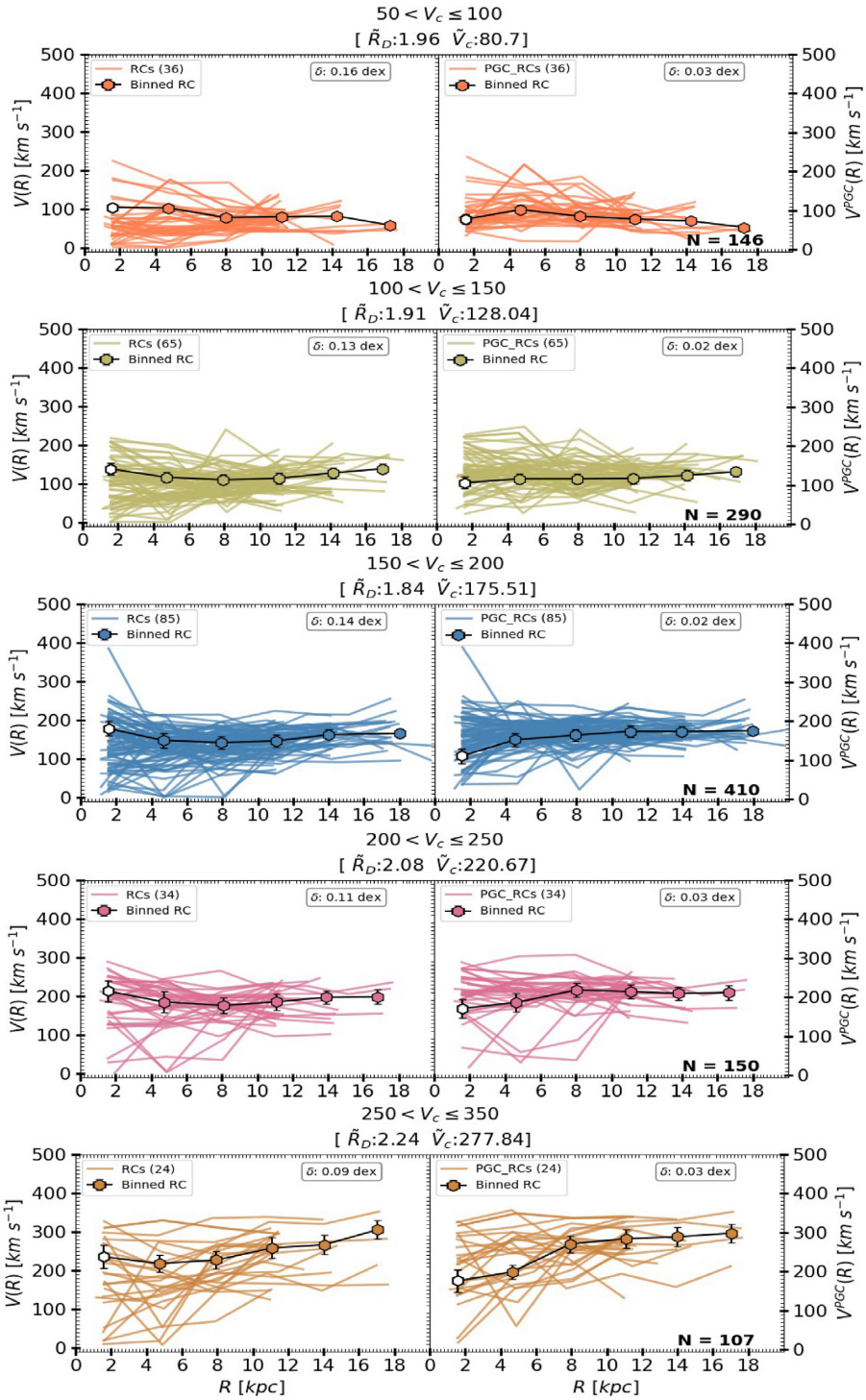

Figure 7. The comparison of non-PGC and PGC co-added RCs (left-hand and right-hand panel, respectively). From top to bottom- bin_50-100: orange colour, bin_100-150: khaki colour, bin_150-200: blue colour, bin_200-250: pink colour and bin_250-350: dark-orange colour. The colour code is same for individual RCs (solid curves/lines) and co-added RCs (black line/curve connected with hexagons). The median disc radii ($\tilde{R}_D$ in kpc) and the median circular velocity ($\tilde{V}_c$ in km s^{-1}) of each bin is displayed in the title of each bin. The digits in the bracket of each legend represent the number of RCs co-added in each bin, and total number of co-added data points per bin are printed in the lower right-hand corner of each plot. The variance in the individual RCs data is given by δ, shown in the rectangular box in the upper right-hand corner of the each plot. Notice, binned data point of first radial bins is within the resolution limit. Hence, to make it clearer to the reader, we show it by open/white hexagon, and discarded in the further analysis of RCs.

Downloaded from https://academic.oup.com/mnras/article/503/2/1753/6128665 by SISSA - Scuola Internazionale Superiore di Studi Avanzati user on 29 March 2021

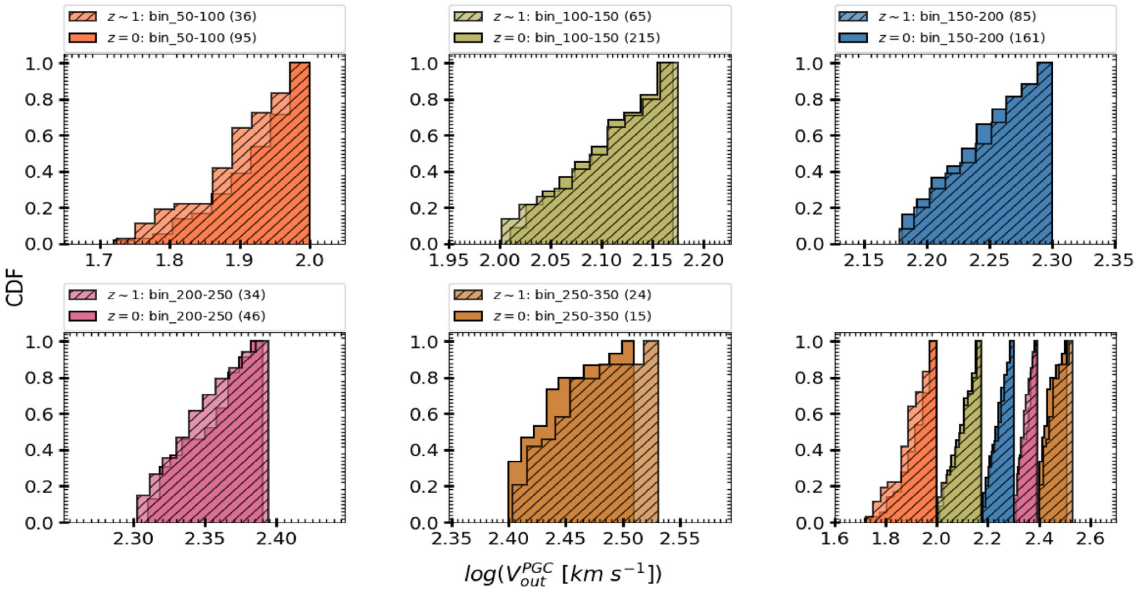

Figure 8. A comparison of cumulative density distribution of circular velocities of $z \sim 1$ (hatched histograms) and $z \approx 0$ (plane histograms) galaxies. The colour code of each bin is same as Fig. 7.

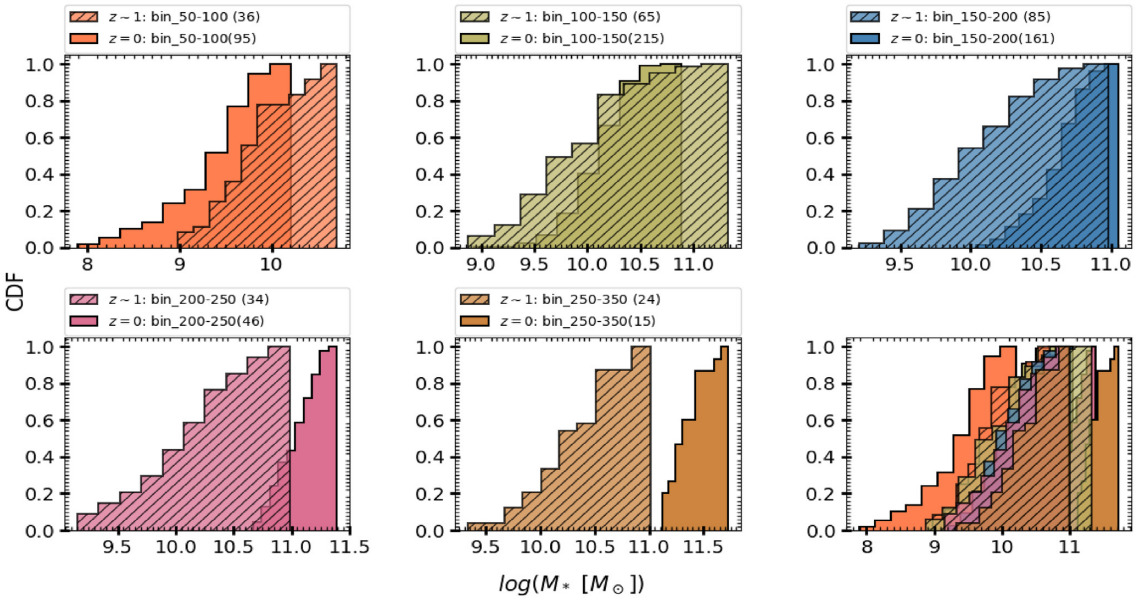

Figure 9. A comparison of cumulative density distribution of stellar masses of $z \sim 1$ (hatched histograms) and $z \approx 0$ (plane histograms) galaxies. The colour code of each bin is same as Fig. 7.

indistinguishable in terms of total mass but differ in stellar masses, an outcome which is expected from the empirical galaxy formation and evolution model (c.f. Moster, Naab & White 2018, and references therein). This implies that we are comparing the local SFGs (disc-type systems), with galaxies at $z \sim 1$ those are most likely their progenitors, in which gas is turning into stars keeping the total mass constant.

Notice, due to low spatial resolution in the inner region ($R <$ 2.5 kpc), we do not draw any conclusion within the effective radii. Moreover, due to the lack of knowledge on gaseous components and the fact that stellar disc scale lengths show no dependence on the circular velocity, we leave the presumably complex process of RC normalization for future work. Hence, in this work, all the RCs are presented in physical units, i.e. km s^{-1} opposed to kpc. Let us finally remark, the model and techniques employed in this work may be subject to some uncertainties, mostly because high-z galaxies may not be fully rotation supported disc galaxies. However, this is a problem for any high-z study and can be mitigated only by acquiring better data, e.g. *JWST*/NIRSpec and ELT/HARMONI as providing more sensitive and higher spatial resolution observations of high-z galaxies.

5 DISCUSSION

Although we are limited by a few caveats mentioned in previous section, we proceed to interpret our results in the context of $z \approx 0$ star-forming discs. In Fig. 10, we show the comparison of our binned RCs (PGC applied) of $z \sim 1$ with the URCs of $z \approx 0$. For the purpose of clear and tidy comparison, we do not show the first radial bin of

Downloaded from https://academic.oup.com/mnras/article/503/2/1753/6128665 by SISSA - Scuola Internazionale Superiore di Studi Avanzati user on 29 March 2021

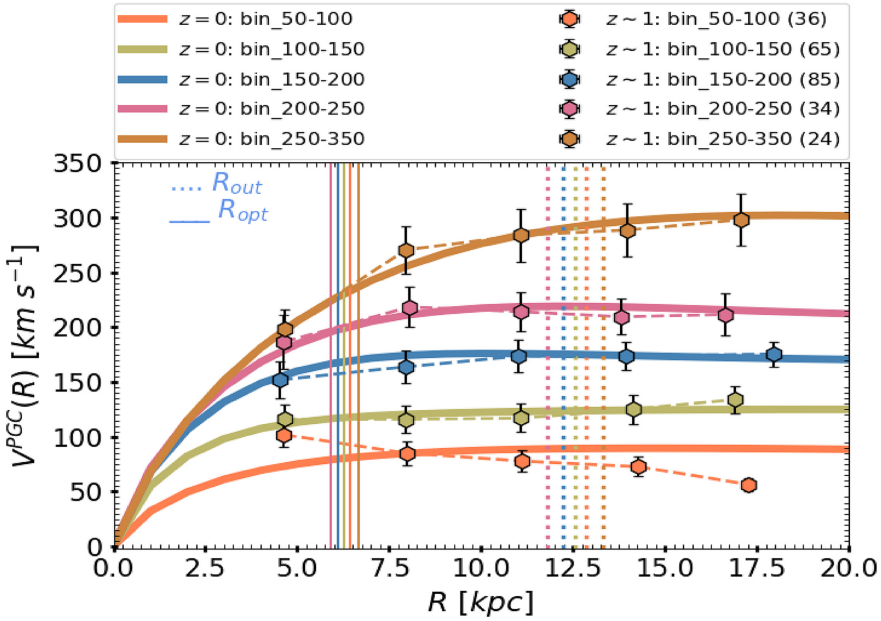

Figure 10. A comparison of $z \sim 1$ co-added RCs of five velocity bins (dashed line connected hexagons) with local RCs (solid curves) of similar velocity bins derived from the URC sample (Persic et al. 1996; Salucci et al. 2007). The colour code of each velocity bin is the same as Fig. 7. The digits in the bracket of the legend represent the number of RCs co-added in each bin. The dotted and solid vertical lines are showing the $R_{\rm out}$ and $R_{\rm opt}$, respectively, for each RC (colour coded same as velocity bins).

each binned RCs. The last radial bins contains the few data points but we keep them in the analysis because they can be informative.[14] We notice that all the $z \sim 1$ RCs coincide with the local RCs from optical radii ($\sim 2R_e$) till the last point of observation. Except the lowest bin (bin_50-100) which shows a gradual decline with increasing radius. In short Fig. 10 is an explicit representation of $z \sim 1$ flat RCs. In the Appendix D1, we also show the co-added RCs in stellar mass bins. We yet again find the flat RCs with relatively large error in the amplitude. On this basis we conclude that the:

(i) SFGs of $z \sim 1$ manifest flat RCs from optical radii ($\sim 2R_e$) till last point of observation.

(ii) Total potential ($\phi(R)$) or total mass within the $\sim$20 kpc radii of $z \sim 1$ and $z \approx 0$ SFGs remains the same, i.e. it did not evolve in the past 6.5 Gyr, which suggests that the DM halo of SFGs most likely evolves slowly by accumulating the matter in the outermost regions of the galaxies. These results concord with the theoretical explanation of Lapi et al. (2020).

Furthermore, we notice a size-evolution in our sample relative to the local late-type galaxies. For the early- and late-type galaxies, size–mass evolution has been already observed and reported in several studies (e.g. van der Wel et al. 2014; Lapi et al. 2018a; Tacconi et al. 2018, and references therein). For an example case, there is an extensive body of work done by van der Wel et al. (2014) on the size evolution of late-type as a function of redshift, where they bin the galaxies in stellar masses and effective radii for redshift range $0.25 \leq z \leq 1.75$. They showed that the size evolution in late-type galaxies could be described as $R_e \propto M_*^{0.22}(1+z)^{-1.48}$. In our work, we are addressing the size evolution in the velocity plane of the $z \sim 1$ galaxies and comparing it with locals, shown in Fig. 11. In particular, we have binned the circular velocities and disc scale length of galaxies for given velocity bins (same as the RCs in Fig. 10), and plotted the stellar disc radii of each velocity bin ($\tilde{R}_D$) as a function of their circular velocities ($\tilde{V}_{\rm out}^{\rm PGC}$). We notice that stellar distribution does not depend on circular velocity. In particular, the lowest velocity bin is consistent with $z \approx 0$ but at a smaller stellar disc-length than $z \sim 1$ on average. On the other hand, we find that with increasing circular velocities, locals are consistent with $z \sim 1$ but contain larger stellar disc-lengths. In short, for the high-z galaxies, the stellar disc radii remains constant as a function of the velocity while for locals it increase. This implies that at $z \sim 1$ the stellar-disc component has not yet established a strong co-relation between the total mass or the total potential of the halo within $\sim$20 kpc as observed in the locals. It could be a consequence of underlying 'complex' astrophysics of the galaxy evolution. For example, most of the baryons are still gaseous at $z \sim 1$, i.e. gaseous-disc dominates. The latter comment has been already mentioned by Glazebrook (2013) and recently deeply investigated and favoured by Tacconi et al. (2018). Here, from the perspective of the dynamics, we emphasize that the stellar mass distribution evolves over cosmic time in the rotation-dominated system, whereas, a negligible evolution is noticed in the lower end of the velocities. Therefore, we suggest that the evolution of stellar light distribution is circular velocity dependent.

[14]For example, RCs of the lowest velocity bin declines at the last (and second last) point of observation, it could be due to very few data points in the last radial bin. However, pay attention to the clear offset in stellar disc scale length in the lowest bin (see Fig. 11), which apparently indicate high stellar-mass objects relative to $z \approx 0$ galaxies (given that $V_c^{z\sim1} < V_c^{z\sim0}$). Therefore, RCs can be declining in the lowest velocity bin. On the other hand, RCs of all the other velocity bins stays flat, even though they contain a few data points in the last radial bins (see Fig. 10).

6 CONCLUSION

In this work, we have analysed the KROSS parent sample (Stott et al. 2016; Harrison et al. 2017). These are IFU based (i.e. 3D data) Hα detected star-forming galaxies at redshift $0.75 \leq z \leq 1.04$. On

Downloaded from https://academic.oup.com/mnras/article/503/2/1753/6128665 by SISSA - Scuola Internazionale Superiore di Studi Avanzati user on 29 March 2021

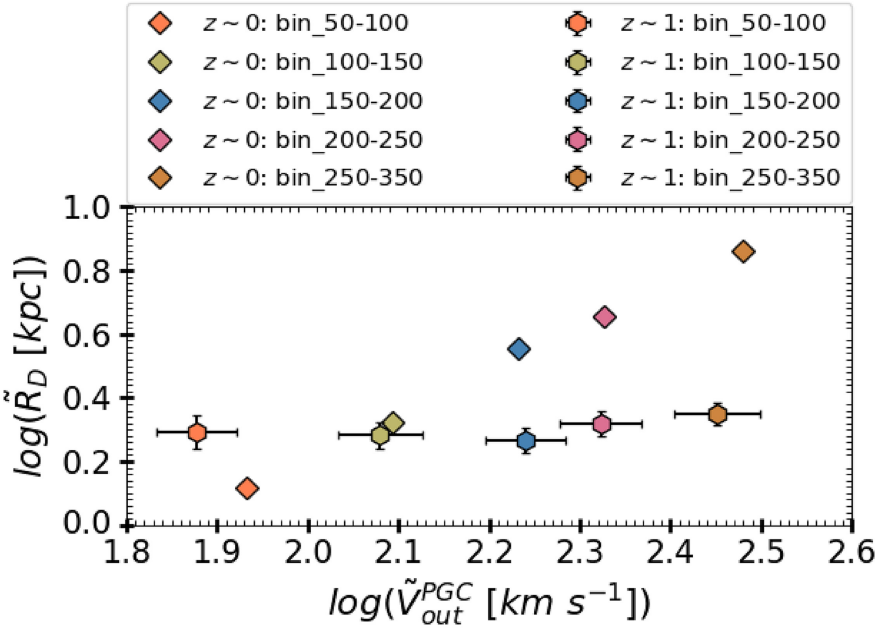

Figure 11. Shows the median stellar disc radii ($\tilde{R}_D$) of each velocity bin as a function of their median circular velocities $\tilde{V}_{\rm out}^{\rm PGC}$. The velocity bins are colour coded similarly as Fig. 10. The hexagons with error bars represents the $z \sim 1$ galaxies and diamonds are showing the local galaxies of similar velocity bin.

the bases of the Hα flux cut ($F_{\rm H\alpha} > 2 \times 10^{-17}$ [erg s^{-1} cm^{-2}]), signal to noise of the Hα detection ($S/N > 3$) and the inclination angle cut ($25^\circ \leq \theta_i \leq 75^\circ$), we have selected 344 galaxies for analysis. We have used the ^{3D}BAROLO (BBarolo) for kinematic modelling of these galaxies, which is also capable of extracting the corresponding rotation curves. The main advantage of this tool is that, it incorporate the beam smearing corrections simultaneously with kinematic modelling in 3D space. Thus it allows us to determine the unbiased rotation velocity and intrinsic velocity dispersion even in the low spatial resolution data. Moreover, we have corrected the RCs for the pressure support applying the PGC, which is discussed in detail in Section 3.2. A 3-fold approach of deriving RCs (3D-kinematic modelling + beam smearing corrections in 3D-space + pressure support corrections), delivers the true intrinsic shape of the RCs (see Fig. 7 right-hand panel and Fig. 10).

We have analysed the 256 rotation-dominated galaxies. This sample covers the redshift range $0.75 \leq z \leq 1.04$, the effective radii $-0.16 \leq \log(R_e\,[\rm kpc]) \leq 0.89$, the circular velocities $1.42 \leq \log\left(V_{\rm out}^{\rm PGC}\ [\rm km\ s^{-1}]\right) \leq 2.57$, and the stellar masses $8.83 \leq \log(M_*\,[\rm M_\odot]) \leq 11.32$. Using the technique of Persic et al. (1996), we have constructed the co-added and binned RCs of the five velocity bins out of 256 individual RCs and compared them with the RCs of local star-forming disc-type galaxies of same velocity bins (see: Section 5 and Fig. 10). The main findings of this work are the following:

(i) The pressure gradient is more dominant effect in high-z galaxies than the beam smearing. It corrects the median rotation velocity more than the 50 per cent, especially in the galaxies with $v/\sigma < 5$.

(ii) A statistically robust method of co-adding and binning RCs shows that the $z \sim 1$ outer RCs are very similar to the outer RCs of the local star-forming galaxies (see Fig. 10) where dark matter dominates and flattens the RCs.

(iii) We have noticed a significant evolution in the disc scale length over past 6.5 Gyr (see Fig. 11).

On the bases of above outcomes, we conclude that the total matter placed in a galactic halo within ∼20 kpc radius at $z \sim 1$ remains same as $z \approx 0$. At the same time, stellar mass distribution (i.e. stellar disc) evolved over cosmic time (in past 6.5 Gyr). This suggests a prolonged evolution of the SFGs (late-type systems).

ACKNOWLEDGEMENTS

We thank the anonymous referees for their constructive comments and suggestions, which have significantly improved the quality of the manuscript. We thank A. Tiley for passing us the SED driven stellar masses of KROSS sample. GS thanks Enrico M. Di Teodoro, M. Petac, and Luigi Danese for their fruitful discussion and immense support in the entire period of this work. GvdV acknowledges funding from the European Research Council (ERC) under the European Union's Horizon 2020 research and innovation programme under grant agreement No. 724857 (Consolidator Grant ArcheoDyn).

DATA AVAILABILITY

In this work, we make use of KROSS data, which is publicly available at KROSS website. A catalogue of 344 KROSS star-forming galaxies used in the work is available at Gauri Sharma Dataverse.

REFERENCES

Arnouts S., Cristiani S., Moscardini L., Matarrese S., Lucchin F., Fontana A., Giallongo E., 1999, MNRAS, 310, 540
Bacon R. et al., 2010, in McLean I. S., Ramsay S. K., Takami H., eds, Proc. SPIE Conf. Ser. Vol. 7735, The MUSE second-generation VLT instrument. SPIE, Bellingham, p. 773508
Begeman K., 1989, A&A, 223, 47
Bosma A., 1981, AJ, 86, 1791
Bosma A., Van der Kruit P., 1979, A&A, 79, 281
Bouché N., Carfantan H., Schroetter I., Michel-Dansac L., Contini T., 2015, AJ, 150, 92
Bruzual G., Charlot S., 2003, MNRAS, 344, 1000

Downloaded from https://academic.oup.com/mnras/article/503/2/1753/6128665 by SISSA - Scuola Internazionale Superiore di Studi Avanzati user on 29 March 2021

Burkert A. et al., 2010, ApJ, 725, 2324 (B10)
Catinella B., Giovanelli R., Haynes M. P., 2006, ApJ, 640, 751
Chabrier G., 2003, PASP, 115, 763
Courteau S., Dutton A. A., 2015, ApJ, 801, L20
Dalcanton J. J., Stilp A. M., 2010, ApJ, 721, 547
Davies R. et al., 2013, A&A, 558, A56
Di Teodoro E., Fraternali F., Miller S., 2016, A&A, 594, A77
Eisenhauer F. et al., 2003, in Iye M., Moorwood A. F. M., eds, Proc. SPIE Conf. Ser. Vol. 4841, Instrument Design and Performance for Optical/Infrared Ground-based Telescopes. SPIE, Bellingham, p. 1548
F'orster Schreiber N. M., Wuyts S., 2020, ARA&A, 58, 661
Freedman W. L., Turner M. S., 2003, Rev. Mod. Phys., 75, 1433
Freeman K., 1970, ApJ, 160, 811
Genzel R. et al., 2017, Nature, 543, 397
Genzel R. et al., 2020, ApJ, 902, 98
Giacconi R. et al., 2001, ApJ, 551, 624
Glazebrook K., 2013, Publ. Astron. Soc. Aust., 30, e056
Harrison C. et al., 2017, MNRAS, 467, 1965 (H17)
Ilbert O. et al., 2006, A&A, 457, 841
Johnson H. L. et al., 2018, MNRAS, 474, 5076
Karukes E. V., Salucci P., 2017, MNRAS, 465, 4703
Kassin S. A. et al., 2007, ApJ, 660, L35
Kassin S. A. et al., 2012, ApJ, 758, 106
Korsaga M., Epinat B., Amram P., Carignan C., Adamczyk P., Sorgho A., 2019, MNRAS, 490, 2977
Kretschmer M., Dekel A., Freundlich J., Lapiner S., Ceverino D., Primack J., 2020, preprint (arXiv:2010.04629)
Lang P. et al., 2017, ApJ, 840, 92
Lapi A. et al., 2018a, ApJ, 857, 22
Lapi A., Salucci P., Danese L., 2018b, ApJ, 859, 2
Lapi A., Pantoni L., Boco L., Danese L., 2020, ApJ, 897, 81
Lawrence A. et al., 2007, MNRAS, 379, 1599
Lehmer B. D. et al., 2005, ApJS, 161, 21
Loiacono F., Talia M., Fraternali F., Cimatti A., Di Teodoro E. M., Caminha G. B., 2019, MNRAS, 489, 681
Moster B. P., Naab T., White S. D. M., 2018, MNRAS, 477, 1822
Padmanabhan T., 1993, Structure Formation in the Universe. Cambridge Univ. Press, Cambridge
Persic M., Salucci P., 1991, ApJ, 368, 60
Persic M., Salucci P., Stel F., 1996, MNRAS, 281, 27
Read J., Iorio G., Agertz O., Fraternali F., 2016, MNRAS, 462, 3628
Reyes R., Mandelbaum R., Gunn J., Pizagno J., Lackner C., 2011, MNRAS, 417, 2347
Rubin V. C., Ford W. K., Jr, Thonnard N., 1980, ApJ, 238, 471
Salucci P., 2019, A&AR, 27, 2
Salucci P., Burkert A., 2000, ApJ, 537, L9
Salucci P., Lapi A., Tonini C., Gentile G., Yegorova I., Klein U., 2007, MNRAS, 378, 41
Scoville N. et al., 2007, ApJS, 172, 38
Sharples R., 2015, in Ziegler B. L., Combes F., Dannerbauer H., Verdugo M., eds, Proc. IAU Symp. 309, Galaxies in 3D across the Universe. Cambridge Univ. Press, Cambridge, p. 11
Simons R. C. et al., 2017, ApJ, 843, 46
Sobral D. et al., 2015, MNRAS, 451, 2303
Sofue Y., Rubin V., 2001, ARA&A, 39, 137
Springel V. et al., 2005, Nature, 435, 629
Steidel C. C., Adelberger K. L., Dickinson M., Giavalisco M., Pettini M., Kellogg M., 1998, ApJ, 492, 428
Stott J. P. et al., 2016, MNRAS, 457, 1888
Tacconi L. J. et al., 2018, ApJ, 853, 179
Tasca L. A. M. et al., 2009, A&A, 503, 379
Teodoro E. D., Fraternali F., 2015, MNRAS, 451, 3021
Tiley A. et al., 2019a, MNRAS, 482, 2166
Tiley A. L. et al., 2019b, MNRAS, 485, 934
Turner O. J., Harrison C. M., Cirasuolo M., McLure R. J., Dunlop J., Swinbank A. M., Tiley A. L., 2017, preprint (arXiv:1711.03604)
Übler H. et al., 2019, ApJ, 880, 48
Valenzuela O., Rhee G., Klypin A., Governato F., Stinson G., Quinn T., Wadsley J., 2007, ApJ, 657, 773
Valotto C., Giovanelli R., 2003, Bol. Asoc. Argentina Astron. Plata Argentina, 46, 97
van der Wel A. et al., 2012, ApJS, 203, 24
van der Wel A. et al., 2014, ApJ, 788, 28
Varidel M. R. et al., 2019, MNRAS, 485, 4024
Wechsler R. H., Tinker J. L., 2018, ARA&A, 56, 435
Weijmans A.-M., Krajnović D., Van De Ven G., Oosterloo T. A., Morganti R., De Zeeuw P., 2008, MNRAS, 383, 1343 (W08)
Wellons S., Faucher-Giguère C.-A., Anglés-Alcázar D., Hayward C. C., Feldmann R., Hopkins P. F., Kereš D., 2020, MNRAS, 497, 4051
Whiting M. T., 2012, MNRAS, 421, 3242
Wisnioski E. et al., 2015, ApJ, 799, 209
Wisnioski E. et al., 2019, ApJ, 886, 124
Yegorova I. A., Babic A., Salucci P., Spekkens K., Pizzella A., 2011, Astron. Nachr., 332, 846

SUPPORTING INFORMATION

Supplementary data are available at *MNRAS* online.

Figure S1. The outputs of the kinematic modelling using ^{3D}BAROLO.

Please note: Oxford University Press is not responsible for the content or functionality of any supporting materials supplied by the authors. Any queries (other than missing material) should be directed to the corresponding author for the article.

APPENDIX A: KINEMATIC AND PHOTOMETRIC POSITION ANGLES

If the position angle is correct, then the kinematic modelling allows us to extract the PV diagram symmetric on the x and y axis, but if PA is wrong, then an asymmetry is spotted in PV diagram (see Fig. A3). For nearly 44 per cent objects PA_{phot} do not coincide with

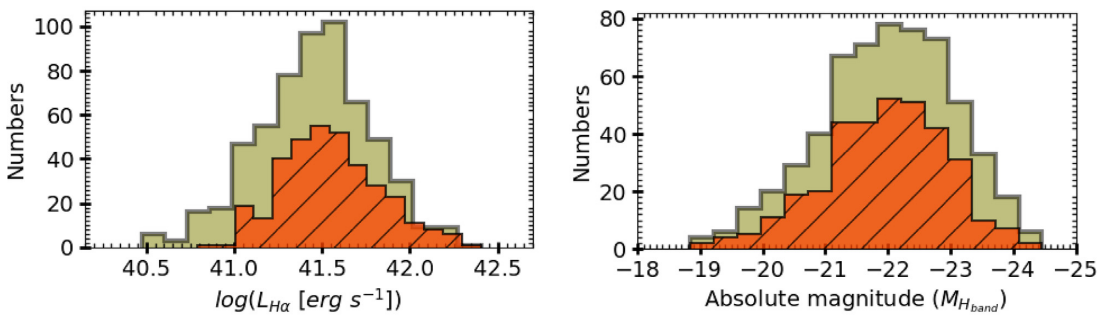

Figure A1. Fig. 1 continued. Left-hand panel: Hα luminosity, Right-hand panel: H-band absolute magnitude.

Downloaded from https://academic.oup.com/mnras/article/503/2/1753/6128665 by SISSA - Scuola Internazionale Superiore di Studi Avanzati user on 29 March 2021

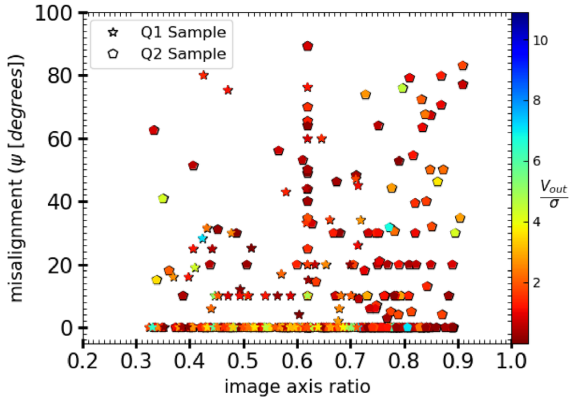

Figure A2. The difference between the photometric and kinematic position angles (ψ) as a function of broad-band image axial ratio. The stars and hexagons represents the Q1 and Q2 sample, respectively, colour coded for v/σ. Nearly 3.5 per cent Q1-sample and 13.3 per cent Q2-sample have misalignment more than $\psi > 30^\circ$. Overall 83 per cent Q12-sample have good position angles measures (i.e. $PA_{phot} \simeq PA_{kin}$) which places confidence on our measurements.

PA_{kin}. Therefore we decided to free the PA parameter in BBarolo-run particularly for these objects. The BBarolo estimated PA are referred to as PA_{kin} in the analysis and flagged in the given catalogue (Table E1). An example of kinematic modelling using PA_{phot} (when it is wrong) and PA_{kin} is shown in Fig. A3. Upper panel shows the kinematics and rotation curve derived using PA_{kin}, whereas lower panel shows the kinematics and rotation curve derived from fixed PA_{phot}. We can see that PV diagrams drove from fixed PA_{phot} are asymmetric around x and y axis, while this problem resolved if the PA is set to free in BBarolo run. We are not keeping PA free for all objects because BBarolo documentation suggests to 'keep the number of free parameter low, specifically in low-resolution data'.

A1 Photometric and kinematic major axes

Here, we discuss the misaligned kinematic and photometric (morphological) major axes. As we mentioned in the Section 3.1.2, nearly 44 per cent of analysed sample have $PA_{phot} \neq PA_{kin}$. This discrepancy in the position angles can affect our results in two ways: (1) uncertain inclination angle because inclination is derived using photometric axial ratio, which is used in computing PA_{phot} too (see Section 2.2) and (2) presumably misaligned systems are not in disc configuration, which is worrisome. Therefore, we quantitatively explored the misalignment in the Q12 sample. Following Wisnioski et al. (2015), we define the misalignment between photometric and kinematic position angle as

$$\sin\psi = |\sin(PA_{phot} - PA_{kin})|, \tag{A1}$$

where ψ gives the misalignment and lies between 0° and 90°. If $\psi > 30^\circ$ than morphologies are considered irregular. Fig. A2 shows the ψ as a function of image axial ratio, where axis ratios are derived using broad-band images (for details see Harrison et al. 2017). We notice, ∼ 40 per cent objects of Q12-sample are misaligned, in which only ∼ 17 per cent objects have $\psi > 30^\circ$ (which includes ∼ 3.5 per cent Q1 sample and ∼ 13.3 per cent Q2 sample). We notice low v/σ galaxies are highly misaligned, most likely due to lack of well-defined kinematic axis. Despite the different kinematic modelling approaches, our misalignment results are similar to Harrison et al. (2017). Moreover, majority (∼ 83 per cent) of our sample used in RCx analysis (Q12 sample), have $PA_{phot} \simeq PA_{kin}$ which places confidence on our measurements. Besides it, we provide a statistical study of RCs which encompass any uncertainties caused by misalignment.

Furthermore, our main results (see Fig. 10) show that the co-added RCs of our sample ($z \sim 1$) coincides with the RCs of local disc galaxies with a precision of more than 95 per cent. Therefore, we infer that the majority ($\gtrsim$ 83 per cent) of our galaxies are in disc-like configuration.

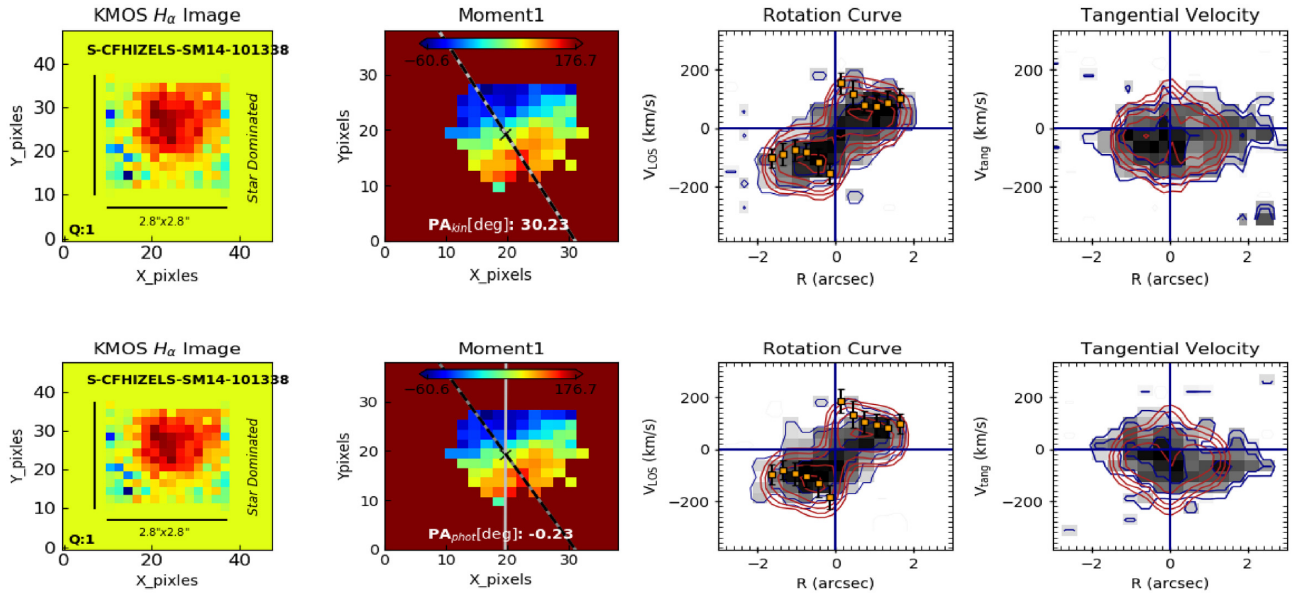

Figure A3. Upper panel: Kinematic modelling using PA_{kin}. Lower panel: Kinematic modelling performed using PA_{phot}. COL 1: Integrated H α-image from 3D datacube; COL 2: Rotation velocity map, where PA_{kin} is shown by dotted dashed black-grey line, and PA_{phot} is shown by solid grey line; COL 3: LOS rotation velocity curve; COL 4: Tangential velocity profile. In the PV diagrams, the black shaded area with blue contour represents the data, the red contour is model, and orange squares with error bars are best-fitting velocity measurements.

Downloaded from https://academic.oup.com/mnras/article/503/2/1753/6128665 by SISSA - Scuola Internazionale Superiore di Studi Avanzati user on 29 March 2021

APPENDIX B: EXAMPLES OF PRESSURE GRADIENT CORRECTIONS

Some examples of PGC on the BBarolo generated rotation curves are shown in the Figs B1 and B2.

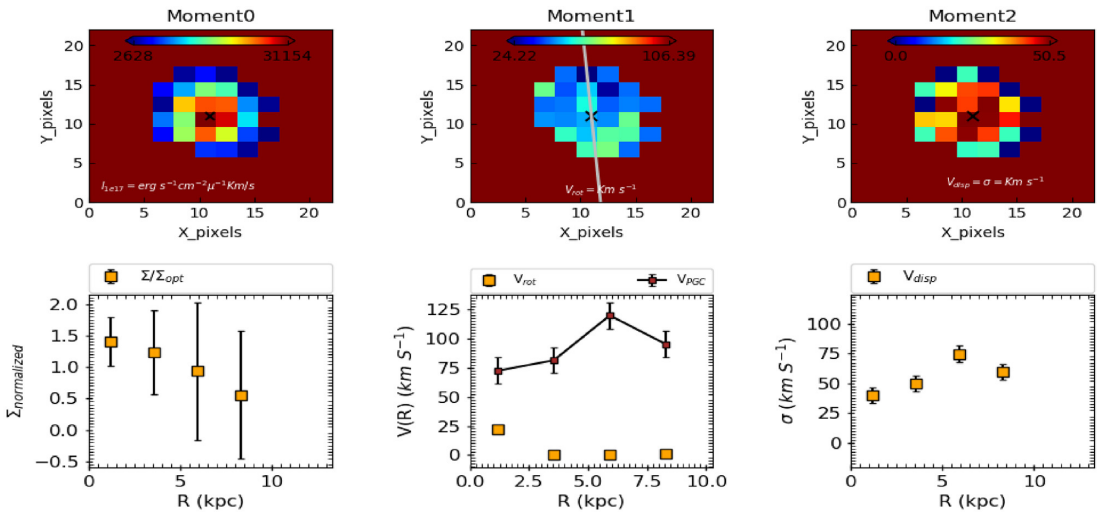

Figure B1. An example of PGC. Upper panel: left-to-right, zeroth, first, and second moment maps. Lower panel: left-to-right, the surface brightness, the rotation velocity, and the velocity dispersion. In the moment-1 map, the grey line is the photometric position angle and the black cross are the galactic kinematic centre (x_c^k, y_c^k). In the surface brightness profile and the P–V diagrams, the orange squares with error bars are best fit data. In the rotation curve profile, brown squares connected with the black line is PG corrected rotation velocity profile.

Downloaded from https://academic.oup.com/mnras/article/503/2/1753/6128665 by SISSA - Scuola Internazionale Superiore di Studi Avanzati user on 29 March 2021

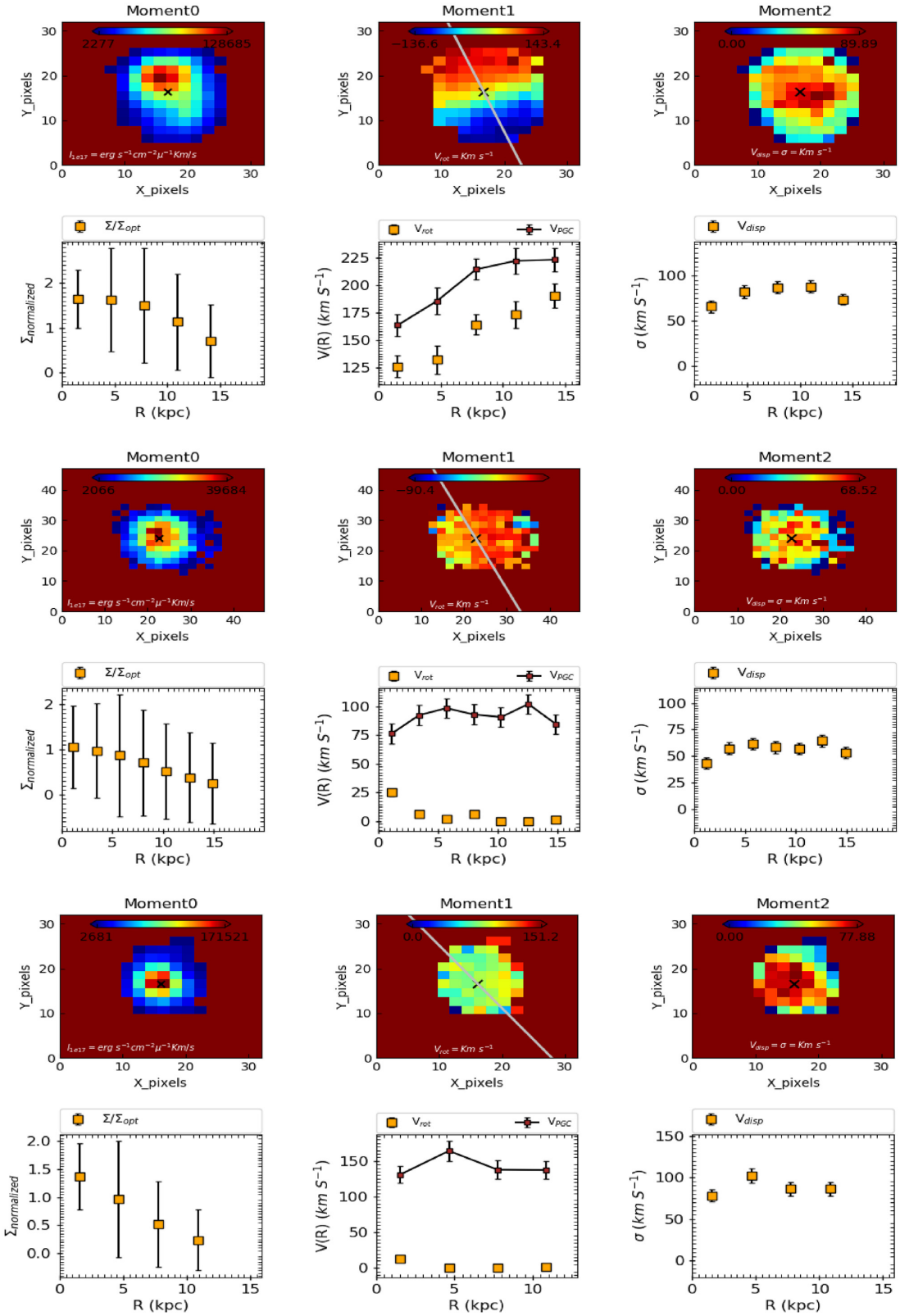

Figure B2. PGC examples continue...

Downloaded from https://academic.oup.com/mnras/article/503/2/1753/6128665 by SISSA - Scuola Internazionale Superiore di Studi Avanzati user on 29 March 2021

APPENDIX C: PRESSURE GRADIENT CORRECTIONS WITH CONSTANT σ

We compare our PGC following the Weijmans et al. (2008, hereafter W08) with the often adopted PGC following Burkert et al. (2010, hereafter B10) given by

$$V_c^2(r) = V_0^2(r) + 2\sigma_0^2 \frac{r}{R_D}, \tag{C1}$$

where V_0 is the inclination corrected rotation velocity when the pressure gradient is negligible, and the velocity dispersion (σ_0) is isotropic and radially constant. In equation (C1) second term gives the pressure term. We have noticed a significant difference in both methods, shown in Fig. C1. In B10 method RC are successively rising, and corrections are always applied even when they are not required. This is due to the constant σ and r/R_D factor, which imposes the circular velocity to increase as a function of radius. On the other hand, W08 method uses the full information available in the datacubes, including the radially varying surface-brightness, rotation velocity, and velocity dispersion. This avoids the un-necessary radially growing circular velocity, as well as, the corrections are only applied if needed. Furthermore, in Fig. C2, we have shown the amount of pressure support correction $\Delta V = V_c^{\rm PGC} - V_c^i$ (computed at $R_{\rm out}$) in both cases as a function of velocity dispersion. We can see that the corrections are twice higher in B10 method than W08, and unrealistically high in low v/σ galaxies.

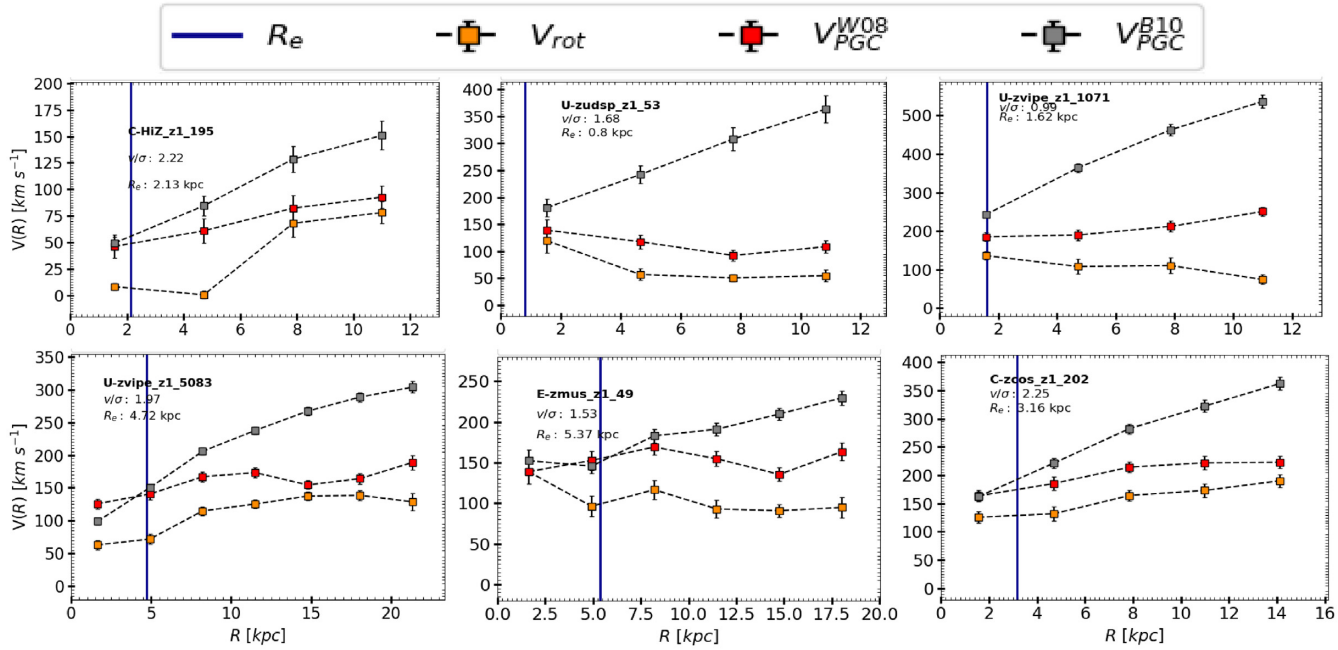

Figure C1. The rotation curves before and after PGC using Weijmans et al. (2008) and Burkert et al. (2010) method. The yellow square represents the intrinsic RC without PGC (denoted by $V_{\rm rot}$). The red and grey square shows the PG corrected RCs using Weijmans et al. (2008) and Burkert et al. (2010) method, denoted by $V_{\rm PGC}^{W08}$ and $V_{\rm PGC}^{B10}$, respectively. The vertical blue line shows the effective radius of the galaxy. The name, v/σ and R_e of galaxies are printed at upper-left corner of each plot.

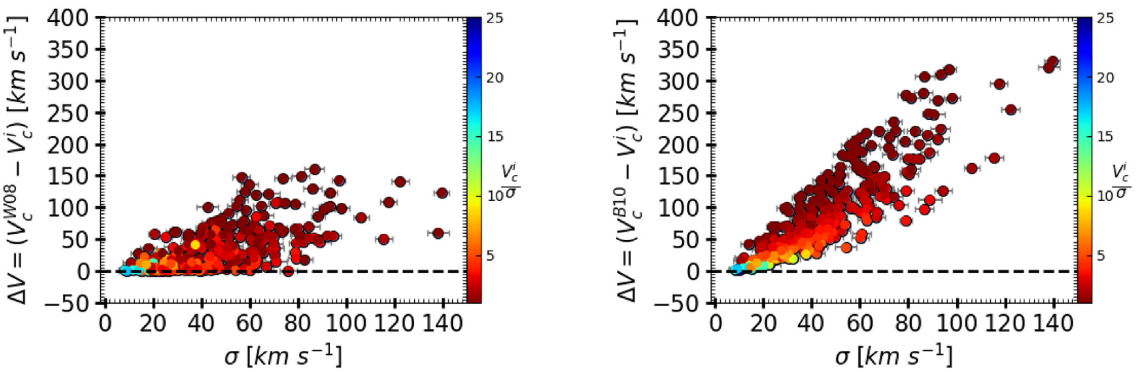

Figure C2. The comparison of correction factor ($\Delta V = V_c^{\rm PGC} - V_c^i$) on rotation velocities before and after the PGC, using Weijmans et al. (2008) and Burkert et al. (2010) method (left-hand and right-hand panel, respectively). The correction factor is plotted as a function of velocity dispersion and data-points are colour coded for V_c^i/σ (i.e. v/σ). The notation of circular velocities are given as follows, V_c^{W08} and V_c^{B10} denotes the PGC using W08 and B10 method, respectively. Whereas V_c^i is the inclination corrected rotation velocity without PGC, computed at $R_{\rm out}$. We notice, pressure correction using B10 method are on an average a factor of 2 higher than W08 method, which is also shown by Kretschmer et al. (2020).

Downloaded from https://academic.oup.com/mnras/article/503/2/1753/6128665 by SISSA - Scuola Internazionale Superiore di Studi Avanzati user on 29 March 2021

Recently, based on high-resolution zoom-in cosmological simulation, Kretschmer et al. (2020) compared the pressure term of jeans/hydrostatic equilibrium (Weijmans et al. 2008) given by

$$\alpha_{\rm true} = -\frac{\partial\, ln\, \rho\, \sigma_R^2}{\partial\, ln\, R} + (1 - \frac{\sigma_\phi^2}{\sigma_R^2}) + \Delta Q,$$

where all the symbols have their usual meaning (as given in Section 3.2) and ΔQ is non-spherical potential term, which we neglect in our work. On the other hand, pressure term in self-gravitating exponential disc (Burkert et al. 2010), given by

$$\alpha_{\rm self} = 2\frac{r}{0.59\, R_e}.$$

Kretschmer et al. (2020) concluded that (1) $\alpha_{\rm self} = 2\alpha_{\rm true}$, (2) pressure correction from non-isotropic and non-constant velocity dispersion are not negligible for gas within $R = R_{e,\,\rm gas}$, and (3) pressure support correction derived from self-gravitating disc assuming constant velocity dispersion is not valid for high-z galaxies. In Fig. C2, we clearly verify their findings. Moreover, since we do not know the exact distribution of gas in high-z. Therefore, we encouraged to avoid any prior assumption on gas component, whether it is related to turbulent pressure or effective radii of gaseous disc ($R_{e,\,\rm gas}$).

APPENDIX D: CO-ADDED RCS OF STELLAR MASS BINS

In Fig. D1, we show the co-added and binned RCs of four stellar mass bins, namely bin_8.5-9.5, bin_9.5-10, bin_10.0-10.5, and bin_10.5-11.5. We yet again find the flat RCs with relatively higher error in the amplitude.

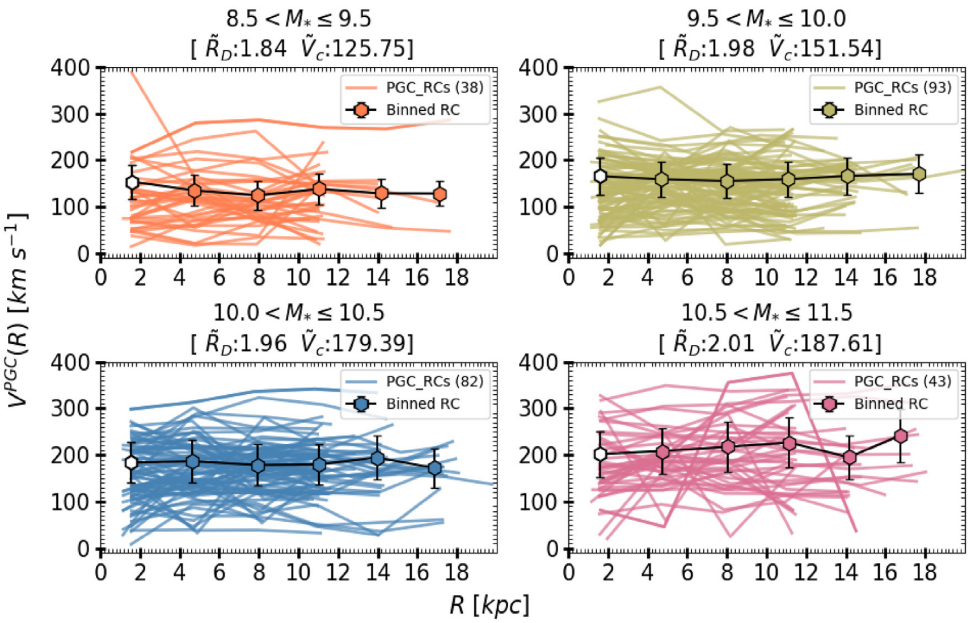

Figure D1. The co-added and binned RCs in the stellar mass bins. The colour code of M_* bins is the following, the orange: bin_8.5-9.5, green: bin_9.5-10, blue: bin_10.0-10.5, and pink: bin_10.5-11.5. The solid lines represents the individual RCs and hexagon connected black curve shows the binned RCs. The procedure of co-adding and binning is same as given in the Section 4.2.

Downloaded from https://academic.oup.com/mnras/article/503/2/1753/6128665 by SISSA - Scuola Internazionale Superiore di Studi Avanzati user on 29 March 2021

APPENDIX E: CATALOGUE

With this paper, we release a catalogue of raw values (adopted from Harrison et al. 2017) and derived values for the 344 KROSS star-forming galaxies used in the work. In Table E1 we describe the columns of the catalogue released with this paper. The full version of Fig. 3 and a machine readable table is attached in the external appendix.

Table E1. Details of the columns provided in catalogue associated with this paper.

Descriptions of columns			
Number	Name	Units	Description
1	KID	–	KROSS ID. (Harrison et al. 2017, hereafter Ref: H17).
2	Name	–	Object Name (Ref: H17).
3	Quality	–	Quality flag for the data (see Section 3.1.4):
		–	Quality 1: H α detected, best moment map and RCs.
		–	Quality 2: H α detected, reasonably good moment map and RCs.
		–	Quality 3: H α detected but bad moment maps and RCs (discarded from the analysis).
4	Flag_*PA*	–	Position angle flag for the data:
		–	kin: Position angle derived from BBarolo Kinematic modelling.
			phot: Photometric position angle (Ref: H17).
5	RA	–	Right Ascension [J2000] (Ref: H17).
6	DEC	–	Declination [J2000] (Ref: H17).
7	z	–	Redshift from H α (Ref: H17).
8	*PA*	degrees	Positional angle (PA).
9	INC	degrees	Inclination angle (Ref: H17).
10	M_H	–	Absolute *H*-band magnitude (Ref: H17).
11	z_AB	–	*z*-band AB-magnitude (Ref: H17).
12	K_AB	–	*K*-band AB-magnitude (Ref: H17).
13–14	Re, Re_err	log (kpc)	Deconvolved continuum half-light radii, $R_{1/2}$, from the image and error (Ref: H17).
15–16	Vout, Vout_err	log (km s^{-1})	Rotation velocity computed at 6.4 R_D ($R_D = 0.59\,R_e$) and error.
17–18	VPGC_out, VPGC_out_err	log (km s^{-1})	PGC corrected rotation velocity computed at 6.4 R_D ($R_D = 0.59\,R_e$) and error.
19–20	sigma, sigma_err	log (km s^{-1})	Weighted mean from intrinsic velocity dispersion profile and error.
21–22	L_Ha, L_Ha_err	log (erg sec^{-1})	Observed H α luminosity and error (Ref: H17).
23	F_Ha	log (erg sec^{-1} cm^{-2})	Observed aperture H α flux (Ref: H17).

This paper has been typeset from a TEX/LATEX file prepared by the author.

Downloaded from https://academic.oup.com/mnras/article/503/2/1753/6128665 by SISSA - Scuola Internazionale Superiore di Studi Avanzati user on 29 March 2021